NTNU – Trondheim
Norwegian University of
Science and Technology

Structural Dynamics of Subsea Structures in Earthquake Prone Regions

Karianne Bruun

Civil and Environmental Engineering
Submission date: June 2013
Supervisor: Ragnar Sigbjørnsson, KT
Co-supervisor: Svein N. Remseth, KT

Norwegian University of Science and Technology
Department of Structural Engineering

Preface

This thesis was written at the Department of Structural Engineering at the Norwegian University of Science and Technology (NTNU) the spring semester of 2013. It represents the work done over a period of 20 weeks and corresponds to 30 credits.

The material presented herein comprises the fields of earthquake engineering, fluid dynamics and structural dynamics. As the author was only familiar with the latter initially, the process has been quite rewarding in terms of learning. Additionally, a respectable amount of time was spent working in Matlab and Abaqus, and surveying what the literature had to offer on the subjects in question.

I would like to thank my supervisors Ragnar Sigbjörnsson and Svein N. Remseth for invaluable help along the way. If not for the discussions regarding theory and problems that emerged during the process, the result would not have been the same.

Secondly, gratitude is extended to Frode Hove, Øivind Matheson Bones and Theresa Böllmann at Reinertsen AS for providing the construction studied in this thesis and all relevant data regarding the structure and the site at which it is located.

Lastly, I would like to thank my family and Tine Olsen Fauskanger for the support and care they have shown during these past 20 weeks.

Trondheim, June 10, 2013

Karianne Bruun

Abstract

With the development that has taken place within the Norwegian oil industry for the past years, both the technology and the challenges have become more complex. Subsea operations have become more common rendering interconnected systems at seabed. In relation to seismic activity this raises the question of whether or not these systems of wells, pipes and other structures are able to withstand an eventual seismic event of a certain magnitude. To take a first step towards answering this question, this thesis covers the study of a protection structure subjected to an acceleration time series found by probabilistic evaluation of selected earthquake data available for the Norwegian continental shelf.

The structure considered is located in the Åsgård field at Haltenbanken west off mid-Norway. It is a rather small and slender construction which function is to protect oil installations from eventual damages caused by trawling or objects falling down in relation to the fishing industry. In the finite element (FE) modelling of this structure it is regarded as a sum of three different systems. The first system is the structural system itself, the second system is the soil system and the third is the fluid system. Thus three models were created in which the different system properties (spings/dashpots, fluid forces) were introduced stepwise.

To investigate the structural response to base accelerations, representative earthquake time histories had to be used. These time histories were found by means of a probabilistic assessment of a synthetic earthquake catalogue. The earthquake catalogue itself was generated by employing the Gutenberg-Richter relation, and the appurtenant parameters and areas for which these hold were found in a seismic zonation report for Norway [4]. The ground motion parameter chosen was the peak ground acceleration in both horizontal and vertical direction estimated by an attenuation relation developed by Ambraseys et. al [6][7]. Further, order statistics was performed on the generated PGAs by employing the Gumbel distribution of maxima. The resulting PGAs in horizontal and vertical direction were then used to find an appropriate time acceleration series in a database containing earthquake data for Europe and the Middle East [5].

Subsequently these acceleration time histories were imposed on the three FE models and the response was evaluated by nonlinear direct implicit integration. Furthermore, a modal analysis was performed on the fully submerged model for comparison reasons. An additional time series was also imposed on the fully submerged model which was generated based on the area with the highest seismic activity found in the zonation report to evaluate the ”worst-case scenario”.

The results of these analyses rendered that with the introduction of soil-structure interaction modelled by springs and dashpots, the displacements generated increased compared to the fixed base model (the structural system). Furthermore, the displacements increased even more with the introduction of fluid forces. Due to small displacements, the inertia forces dominated the overall response of the submerged structure. With reference to structural performance the structure in general was hardly affected by the imposed base accelerations which is a good sign. However, it is hard to conclude from this study how structures like pipes and platforms would have responded to the same base accelerations as these are structures of much larger dimensions and different geometries.

Sammendrag

Med utviklingen som har funnet sted innenfor den norske oljebransjen de siste årene har både teknologien og utfordringene blitt mer komplekse. Subsea-operasjoner har blitt mer vanlig og gir utslag i at det på havbunnen i mange felt er sammenkoblede systemer av konstruksjoner. I relasjon til seismisk aktivitet reises da spørsmålet om disse systemene med brønner, rør og andre konstruksjoner kan tåle å bli utsatt for et jordskjelv av en viss størrelse. For å ta et steg i retningen av å besvare dette spørsmålet, dreier denne hovedoppgaven seg om studien av en beskyttelseskonstruksjon som utsettes for grunnakselerasjoner funnet ved probabilistisk evaluering av valgte jordskjelvdata tilgjengelig for den norske kontinentalsokkelen.

Den valgte konstruksjonen er lokalisert i Åsgårdfeltet på Haltenbanken vest for midt-Norge. Det er en ganske liten og slank konstruksjon hvis funksjon er å beskytte oljeinstallasjoner fra eventuelle skader forårsaket fra tråll og fallende objekter i forbindelse med fiskeriindustrien. I modelleringen av konstruksjonen vurderes den som et produkt av tre forskjellige systemer. Det første systemet er konstruksjonen alene, det andre systemet er jordsystemet og det tredje er fluidsystemet. Dermed ble tre modeller laget der de forskjellige systemegenskapene (fjærer/dempere, hydrodynamiske krefter) ble introdusert stegvis.

For å undersøke konstruksjonens respons i forhold til påsatte grunnakselerasjoner, måtte representative tidsrekker for jordskjelv brukes. Disse tidsrekkene ble funnet ved hjelp av probabilistisk vurdering av en syntetisk jorskjelvkatalog. Denne jordskjelvkatalogen ble generert ved å bruke Gutenberg-Richter relasjonen, og de tilhørende parametrene og områdene de gjelder for ble funnet i en rapport angående seismisk inndeling av Norge [4]. Jordskjelvparameteren som ble valgt var maksimum grunnakselerasjon (PGA) i både horisontal og vertikal retning estimert ved en relasjon funnet av Ambraseys, med flere [6][7]. Videre ble ordningsstatistikk brukt på de genererte PGA-verdiene ved å bruke Gumbels fordeling for maksima. De resulterende PGA-verdiene i horisontal og vertikal retning ble så brukt for å finne en passende tidsrekke for akselerasjon i en database over jordskjelv for Europa og Midtøsten [5]. Deretter ble disse akselerasjonene påsatt de tre modellene og responsen ble evaluert ved ikkelineær direkte implisitt integrasjon. Videre ble en modal analysis av responene utført på den fullt neddykkede modellen for sammenlikningens skyld. Enda en tidsserie ble også påsatt den fullt neddykkede modellen som ble generert basert på det området med høyest seismisk aktivitet, funnet i rapporten nevnt ovenfor for å vurdere det verst tenkelige tilfellet.

Resultatene av disse analysene viste at med introduksjon av jord-konstruksjon-interaksjon modellert ved fjærer og dempere, så økte forskyvningene sammenliknet med den fast innspente modellen (konstruksjonen alene). Videre så økte forskyvningene ytterligere ved å introdusere hydrodynamiske krefter. På grunn av små forskyvninger dominerte treghetskreftene responsen for den neddykkede modellen. Med tanke på konstruksjonens oppførsel så ble konstruksjonen nesten ikke affisert av de påsatte grunnakselerasjonene - som er et godt tegn. Imidlertid er det vanskelig å konkludere hvordan andre typer konstruksjoner som rør og platformer ville ha respondert hvis de ble utsatt for de samme grunnakselerasjonene ettersom disse har mye større dimensjoner og annerledes geometri.

Contents

List of Figures

List of Tables

1 Introduction

1.1 Outline of problem

Since the first drilling operation on the Norwegian continental shelf was performed back in 1966, there has been an exciting development with reference to marine structural engineering [8]. The past years especially, there has been an increasing need for knowledge with reference to subsea structural engineering as the complexity of the oil production conditions have escalated. With complex interconnected systems at the seabed one might begin to wonder how these would respond to strong ground motions.

Ever since the Norwegian oil adventure started there has been no severe accidents reported related to seismic events. There is of course the induced earthquake that occurred in the Ekofisk oil field back in 2001 which was caused by stress changes owing to water injection in a reservoir, but there was no damages on either platforms or wells reported [31]. However, there is likely that oil production will be started in the areas around Jan Mayen which introduce the possibility of seismic activity larger than that experienced in the current producing fields. As there is volcanic activity on Jan Mayen, earthquakes may follow an eventual eruption like the one registered in 1985 where the individual quakes reached a magnitude of 5 [24]. Additionally, the loss connected to an eventual disastrous seismic event is huge with respect to environmental aspects. Thus, the need for seismic knowledge on these areas arises, and earthquake hazard has to be addressed in the design of subsea structural systems in earthquake prone regions.

To investigate the possible effects of a seismic event on subsea structures a study structure provided by Reinertsen AS [2] is modelled in the FEA software Abaqus [18] and ground accelerations found by probabilistic modelling are imposed on the model. Further, the effects of soil-structure interaction and fluid-structure interaction are accounted for and both linear and nonlinear procedures are performed.

1.2 Selection of study case

To investigate how fully submerged structures respond to earthquake excitations, a proper study structure had to be selected. Due to the vast amount of research presented with reference to large scale constructions like platforms and pipes, it was the author's wish to investigate a different kind of structure. Reinertsen AS [2] proposed a protection structure, which is a common construction used by the Norwegian offshore industry. A picture of the structure chosen is shown below in figure 1.

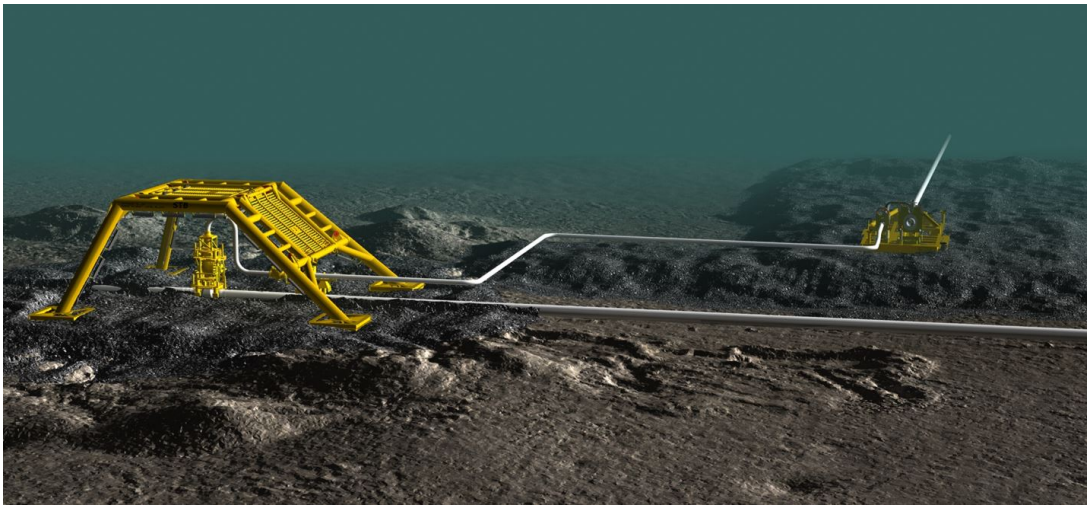

Figure 1: Graphical illustration of the study case employed in this thesis [2].

As can be seen from figure 1 the structure is mainly a three-dimensional frame with a top hatch and an inclined hatch. The function of this structure is to protect oil installations from objects that may fall down, trawl and other possible dangers that may occur in relation to the fishing industry. Its dimensions are quite small compared to other offshore structures, but as the main goal is to investigate the effects of seismic excitations on structures in a marine environment it is considered as an appropriate choice of study case.

1.3 Literature survey

Within the field of earthquake engineering the amount of available literature is quite comprehensive. Referring to Norway there exists a moderate amount of data on seismic activity [4] which is natural as Fennoscandinavia is located in an intra-plate region. However, there has been written a lot of articles on the subject. This is in many ways due to the development over the years within the offshore industry. As the oil production industry became a huge source of economical income for Norway, the Norwegian Petroleum Directorate decided that the seismic hazard analyses were to be conducted for all facilities [9], and thus the field of earthquake engineering and seismic hazard assessment became of interest for the Norwegian engineering community. For example, there has been proposed earthquake time histories for offshore constructions [34] and attenuation models regarding the estimation of peak ground acceleration (PGA) and spectral acceleration (SA) for Norway [19], and there are several other articles published on the topic.

Further, in order to assess seismic hazard, projects regarding the division of areas into seismic hazard zones have been performed - so called seismic hazard mapping. The SHARE project (Seismic Hazard Harmonization in Europe) is one of them. This project concerns the Euro-Mediterranean region, and it presents more than sixty time-independent maps with exceedance probabilities spanning from 10^{-1} to 10^{-4} yearly probability [3]. A similar project is the GEM project (Global Earthquake Model). This project aims to encourage global cooperation with reference to earthquake engineering by sharing data and knowledge [1] which could be useful when thinking of how natural disasters have become more of a global problem rather than only the problem of the affected region.

1.4 Objectives and research questions

As the author is a student within the field of structural engineering with little experience with reference to both practical earthquake engineering and fluid dynamics, there are two main research questions that will be addressed in this thesis:

1. Are strong ground motions a problem on the Norwegian continental shelf with respect to offshore operations?
2. How do fully submerged structures respond to earthquake excitations compared to onshore structures?

And for the same reasons as stated above, a secondary objective is presented which is of a more personal character. This objective is to acquire knowledge on the following engineering topics:

- Earthquake engineering in general.
- Probabilistic approach to simulation of earthquakes.
- Fluid dynamics.

This objective will not be addressed in the same manner as the research questions, as it in fact is not a research question, but it will be addressed in form of the theory presented.

1.5 Limitations and organization of the thesis

This thesis was produced over a period of five months, and as the author possessed little knowledge on both earthquake engineering and fluid dynamics initially, a lot of time has been spent searching the literature and trying to comprehend both details and the macro-scopic picture of both fields, and trying to weed out what is significant in this context, and what is not. Therefore, the material presented here may seem trivial to the experienced engineer, but in the author's experience it represents a whole new database of knowledge.

The thesis is organized in the following way:

- **Chapter 1** is an introductory chapter which aims to present the thesis in short terms and demonstrate the need for knowledge on earthquake engineering within the offshore industry.
- **Chapter 2** presents the relevant theory used in this thesis. The first section is a general introduction to the three major systems that describe a fully submerged structure subjected to ground motions: The structural system, the soil system, and the fluid system. The second section is dedicated to presenting two powerful tools in predicting the response of a structure subjected to base accelerations; the modal analysis and the method of direct implicit integration.
- **Chapter 3** describes the method used in order to find representative earthquake time histories for the site of the chosen construction. Section one comprises the generation of a synthetic earthquake catalogue, section 2 describes the attenuation model employed, section 3 is dedicated to the use of order statistics and de-aggregation while section 4 presents the resulting acceleration time histories.
- The study case is presented in **chapter 4**. Here, section 1 is a general introduction to the properties of the structure, whereas section 2 describes the modelling of this structure in Abaqus [18].
- The results of the analyses performed are presented in **chapter 5** along with an introductory discussion on the probabilistic method used to find the earthquake time series.
- Finally, **chapter 5** provides some concluding remarks on the material presented in this thesis and proposes some recommendations with reference to further studies.

Appendix A presents theory related to the probabilistic approach, whereas the following appendices, B-F, contains the results of the analyses performed. Further, as there exists and digital attachment to the thesis, this attachment is described in appendix G.

2 Theory

2.1 Systems modelling

When designing a construction, the engineer will in most cases have to find an approximate solution to what in reality is a complex problem. Dividing this problem into several sub-problems makes it easier to comprehend what can be expected, and in the end merge these sub-solutions to get an idea on how the construction will behave during a certain event. With the development within the oil industry there has been an increasing need for knowledge with reference to how structural systems behave at the seabed. As the author sees it there are three main "systems" governing the response of a sub-sea structure when subjected to strong ground motions; the structural system itself, the soil system and the fluid system. The environments and the appurtenant properties for a structure subjected to strong ground motions at the base in these environments will in the following be derived for the three systems. If not specified otherwise, the theory in section 2.1.1 is taken from Chopra [15], while the theory in sections 2.1.2 and 2.1.3 is taken from Kramer [25] and Wilson [37], respectively.

2.1.1 Structural System

Consider a multi-degree-of-freedom (MDOF) system subjected to time-varying, tri-axial base accelerations, $\ddot{\mathbf{u}}_g(t)$. By D'Alembert's principle the dynamic system is in equilibrium at all times with inertia forces included. The equation of motion thereby takes the form:

$$\mathbf{M}\ddot{\mathbf{u}} + \mathbf{C}\dot{\mathbf{u}} + \mathbf{K}\mathbf{u} = \mathbf{P}_{\text{eff}}(t) \tag{2.1.1}$$

Here $\mathbf{M}$, $\mathbf{C}$ and $\mathbf{K}$ are the mass, damping and stiffness matrices of the structure, respectively, whereas $\ddot{\mathbf{u}}(t)$, $\dot{\mathbf{u}}(t)$ and $\mathbf{u}(t)$ are the accelerations, velocities and displacements of the structure relative to the ground. Denoting $\mathbf{P}_{\text{eff}}(t)$ the effective earthquake load these are derived by viewing the total displacement of each mass, $\mathbf{u}^t(t)$ as a combination of its displacement due to static ground motion application, $\mathbf{u}^s$, and its dynamic displacement relative to the quasi-static displacement, $\mathbf{u}$:

$$\mathbf{u}^t(t) = \mathbf{u}^s(t) + \mathbf{u}(t) \tag{2.1.2}$$

The quasi-static displacement can further be described by the use of an influence matrix, $\mathbf{L}$. This matrix relates the quasi-static displacements to the ground displacements, and as its name indicates, it describes the influence of the support displacements on the structural displacements [35]:

$$\mathbf{u}^s(t) = \mathbf{L}\mathbf{u}_g(t) \tag{2.1.3}$$

With the use of this influence matrix the effective earthquake load will take the form

$$\mathbf{P}_{\text{eff}}(t) = -\mathbf{M}\mathbf{L}\ddot{\mathbf{u}}_g(t) \tag{2.1.4}$$

and the resulting equation of motion for and MDOF system subjected to tri-axial base accelerations, $\ddot{\mathbf{u}}_g(t)$ will be:

$$\mathbf{M}\ddot{\mathbf{u}} + \mathbf{C}\dot{\mathbf{u}} + \mathbf{K}\mathbf{u} = -\mathbf{M}\mathbf{L}\ddot{\mathbf{u}}_g(t) \tag{2.1.5}$$

It is here assumed that the strong motion is the only external influence on the system. If additional external loads, $\mathbf{P}(t)$, are to be applied these would of course appear on the right hand side of equation 2.1.5.

2.1.2 Soil system

Concept and implications

The idea of ground motion causing vibrations in a construction during an earthquake is common knowledge. However, the fact that the construction itself interacts with, and also inflicts vibrations in the ground as a response to the ground motion have become an important factor to consider in structural design. This special field within earthquake engineering is known as *soil-structure interaction* (SSI), and its concept and implications will be shortly presented in this section.

When there are no structures present, the ground motions are referred to as *free-field motions*. For example, when the foundation upon which the structure is situated is composed of solid rock, the high stiffness of the rock is little affected by the response of the structure so that the ground motions are approximately the same as the free-field motions. The response of these types of systems is a bit easier to compute compared with those where SSI have effects on the structural response, and they are regarded as *fixed-base structures*.

However, this is not the case if the ground is considered as soft soil. The motion of the foundation at the base of the structure will deviate from the free-field motion because the foundation is unable to adjust to the deformations of the free-field motion. Further on, the dynamic response of the structure to the ground motion will in turn cause deformations in the foundation.

It is obvious that the nature of the SSI during an earthquake is impossible to predict, but its known effects can be accounted for when designing constructions. The main effects of SSI are as follows:

- To reduce the natural frequency of the system so that its value will be lower than if it was a fixed-base structure.
- To increase the effective damping ratio so that its value is greater than that of the structure itself.
- Overall, the demands on the structure tends to reduce due to SSI, while the overall displacements increase.

As stated by Johnson [14], and as one can deduce from the above, the type of structure and its foundation is the critical factors with regards to the importance of SSI. SSI can usually be ignored for most structures, but still it is important to evaluate the problem at hand in order to avoid being excessively conservative. In short terms, the most vulnerable systems to SSI effects are those where the structure is massive and stiff with mat foundations or foundations stiffened by the load-resisting system of the structure; systems such as nuclear power plants for instance.

Methods to accomodate SSI

To analyse SSI, there are mainly two main approaches that stand out today: the *direct methods* and the *multistep methods*. Another approach is to use massless springs at the base of a structure and suitable free-field motions which by paraphrasing Wilson [36]: "... are the only modelling assumptions required to include site and foundation properties in the earthquake analysis of most structural systems".

Direct method

In the direct method the analysis is performed in one step on the entire system including the structure itself and the foundation upon which it is located. The free-field accelerations are applied at the boundaries of the foundation, that is, on the sides and at the base as shown in figure 2 below.

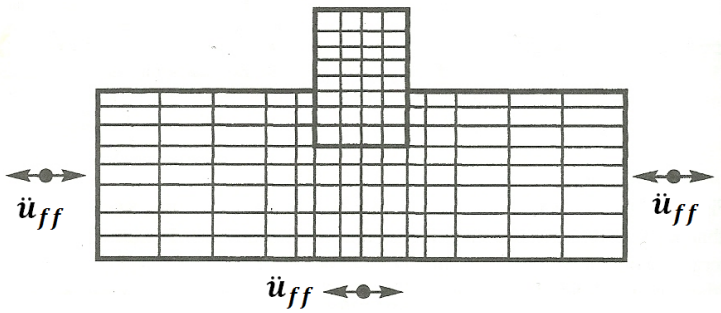

Figure 2: Illustration of the direct method [25].

The response for a finite element model of this system is governed by the following equation of motion

$$\mathbf{M}\ddot{\mathbf{u}} + \mathbf{C}\dot{\mathbf{u}} + \mathbf{K}\mathbf{u} = -\mathbf{M}\ddot{\mathbf{u}}_{\mathrm{ff}}(t) \tag{2.1.6}$$

Here, $\mathbf{M}$ denotes the mass matrix, $\mathbf{C}$ the damping matrix, and $\mathbf{K}$ the stiffness matrix of the entire foundation-structure system. The accelerations, velocities and displacements of the system are denoted $\ddot{\mathbf{u}}$, $\dot{\mathbf{u}}$ and $\mathbf{u}$ whereas $\ddot{\mathbf{u}}_{\mathbf{ff}}(\mathbf{t})$ is the specified free-field accelerations applied at the boundary nodal points. This method demands that the program used for the analysis can treat the behaviour of both structure and foundation correctly even though the stiffness of the two is the same. Also, for large systems it is obvious that this

procedure requires a robust program and some computer power compared with other, more simplified methods.

Multistep mehods

The multistep methods can only be applied to analysis of linear systems as it relies on the principle of superposition. The inability of the foundation to match the free-field deformations is separated from the dynamic response of the structure and the foundation on the supporting soil, and the results are then combined.

If the foundation system impedes the development of free-field motions, its motions will be influenced by *kinematic interaction*, even if the foundation is considered massless. This interaction can in addition result in different modes of vibration in the structure.

The equations of motion for the deformations caused by kinematic interaction are based on the assumption that the foundation is massless as illustrated in figure 3:

$$\mathbf{M}_{\text{soil}}\ddot{\mathbf{u}}_{\text{KI}} + \mathbf{C}\dot{\mathbf{u}}_{\text{KI}} + \mathbf{K}\mathbf{u}_{\text{KI}} = -\mathbf{M}_{\text{soil}}\ddot{\mathbf{u}}_b(t) \tag{2.1.7}$$

where the mass matrix $\mathbf{M}_{\text{soil}}$ is constructed assuming that the structure and foundation are massless, and $\mathbf{C}$ and $\mathbf{K}$ are the damping and the stiffness matrix of the system. The motion of the system is characterized by $\ddot{\mathbf{u}}_{\text{KI}}$, $\dot{\mathbf{u}}_{\text{KI}}$ and $\mathbf{u}_{\text{KI}}$ which are the acceleration, velocity and displacement, whereas $\ddot{\mathbf{u}}_b(t)$ is the acceleration applied at the base of the system. The displacement, $\{\mathbf{u_{KI}}\}$, is called the *foundation input motion* and is the output of equation 2.1.7.

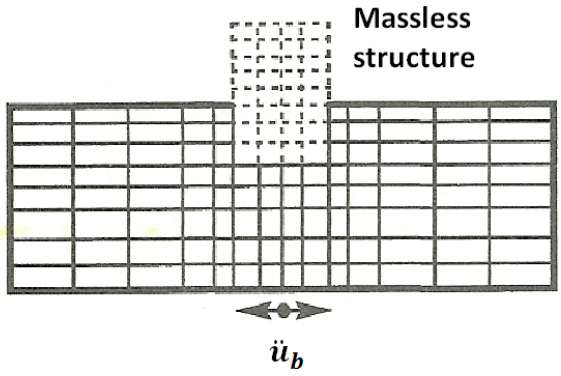

Figure 3: Massless foundation for kinematic interaction analysis [25].

The dynamic response on the supporting soil will further be taken into account by introducing *inertial interaction* as the structure and the foundation are indeed not massless as illustrated in figure 4 below.

If the soil is compliant, the motion of the foundation will be influenced by the dynamic forces acting on the soil as a result of the dynamic response of the structure. The equations of motion for the deformations caused by inertial interaction are as follows:

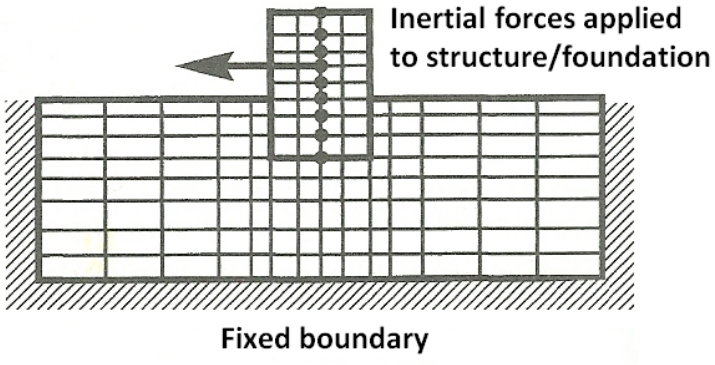

Figure 4: Inertial forces introduced in inertial interaction analysis [25].

$$\mathbf{M}\ddot{\mathbf{u}}_{\mathrm{II}} + \mathbf{C}\dot{\mathbf{u}}_{\mathrm{II}} + \mathbf{K}\mathbf{u}_{\mathrm{II}} = -\mathbf{M}_{\mathrm{structure}}\left(\ddot{\mathbf{u}}_{\mathrm{KI}}(t) + \ddot{\mathbf{u}}_{\mathrm{b}}(t)\right) \tag{2.1.8}$$

where the mass matrix $\mathbf{M}$ represents the mass of the entire system, the mass matrix $\mathbf{M}_{\mathrm{structure}}$ is constructed on the assumption of massless soil, the accelerations, velocities, and deformations $\ddot{\mathbf{u}}_{\mathrm{II}}$, $\dot{\mathbf{u}}_{\mathrm{II}}$ and $\mathbf{u}_{\mathrm{II}}$ are due to inertial interaction, and the acceleration $(\ddot{\mathbf{u}}_{\mathrm{KI}}(t) + \ddot{\mathbf{u}}_{\mathrm{b}}(t))$ is due to both kinematic interaction and motion at the base of the structure. The inertial loading on the structure is represented on the right hand side of equation 2.1.8 and as it can be seen, it depends on the base motion and the foundation input motion while the base of the soil deposit is assumed to be stationary.

If we then add the motion of the massless foundation-structure system due to kinematic interaction to the motion of the foundation-structure system on the massless soil produced by the inertial loading we get the equation of motion for the total system. Adding equation 2.1.7 to equation 2.1.8 we get on the left hand side of the equations of motion:

$$\mathbf{M}_{\mathrm{soil}}\ddot{\mathbf{u}}_{\mathrm{KI}} + \mathbf{M}\ddot{\mathbf{u}}_{\mathrm{II}} + \mathbf{C}\left(\dot{\mathbf{u}}_{\mathrm{KI}} + \dot{\mathbf{u}}_{\mathrm{II}}\right) + \mathbf{K}\left(\mathbf{u}_{\mathrm{KI}} + \mathbf{u}_{\mathrm{II}}\right) \tag{2.1.9}$$

The resulting right hand side will in turn become:

$$-\left(\mathbf{M}_{\mathrm{soil}} + \mathbf{M}_{\mathrm{structure}}\right)\ddot{\mathbf{u}}_{\mathrm{b}}(t) - \mathbf{M}_{\mathrm{structure}}\ddot{\mathbf{u}}_{\mathrm{KI}}(t) \tag{2.1.10}$$

Summarized, the solutions of the kinematic and inertial interaction analysis added provides a solution to the SSI problem at hand since the total motions and the total mass matrix is defined as

$$\mathbf{u} = \mathbf{u}_{\mathrm{KI}} + \mathbf{u}_{\mathrm{II}} \tag{2.1.11a}$$

$$\mathbf{M} = \mathbf{M}_{\mathrm{soil}} + \mathbf{M}_{\mathrm{structure}} \tag{2.1.11b}$$

Inserting equation 2.1.11 into the equations 2.1.9 and 2.1.10, we obtain the resulting equations of motion:

$$\mathbf{M\ddot{u}} + \mathbf{C\dot{u}} + \mathbf{Ku} = -\mathbf{M\ddot{u}}_{\mathrm{b}}(t) \tag{2.1.12}$$

Hence, the superposed solutions add up to the equations of motion of the original systems. An equivalent procedure is to apply springs and dashpots in the inertial interaction analysis for the soil, if the foundation is rigid.

Use of springs

An approximate solution to dealing with SSI is to replace the soil with virtual masses fixed to the foundation, and massless springs and dashpots in parallel with each other for each degree of freedom to ensure correct coupling between the different degrees of freedom [29]. The properties of these elements can be extracted from separate finite element studies, or they can be represented by the half-space equations for circular plates provided in 1 adapted from *Fundamentals of earthquake engineering* [29].

Table 1: Stiffnesses, virtual masses, and dashpot constants for half-space model for a circular base [29].

Degree of freedom	Height of soil prism	Dashpot constant	Stiffness
Vertical	$0.27\sqrt{A}$	$5.42\sqrt{K\rho h^3}$	$\dfrac{4Gr}{1-\nu}$
Horizontal	$0.05\sqrt{A}$	$41.1\sqrt{K\rho h^3}$	$5.8\pi Gr\dfrac{(1-\nu^2)}{(2-\nu)^2}$
Rotation	$0.35\sqrt{A}$	$0.97\sqrt{K\rho h^5}$	$2.7Gr^3(\nu=0)$
Torsion	$0.25\sqrt{A}$	$3.76\sqrt{K\rho h^5}$	$\dfrac{16Gr^3}{3}$

Here, A represents the base area, r the radius, K the stiffness, ρ the mass density of the soil, and h the height of the soil prism. Further, G is the shear modulus and ν is Poisson's ratio of the soil.

Other spring/dashpot-models for modelling SSI are also available. Wolf and Deeks [38] for instance presents the use of a cone and spring-dashpot-mass model for a foundation on the surface of a homogeneous halfspace, while Villaverde [35] presents halfspace spring constants for rigid, flexible and parabolic footings. The subject of different types of spring-dashpot models will not be further addressed in this context, but the subject of the variables used in these models will be shortly discussed.

The shear modulus of soil can be expressed by the shear wave propagation velocity of the soil, V_s, as [36]:

$$V_s = \sqrt{\frac{G}{\rho}} \tag{2.1.13}$$

As can be seen from the spring-dashpot model given by table 1 and equation 2.1.13 the stiffness and damping properties of the system will increase with increasing shear wave velocity. This implies that as V_s increases, the properties of the system will approach the properties of an equivalently fixed base system. Further, Eurocode 8 [30] relates different ground types to shear wave velocities as shown in table 2. Here $V_{s,30}$ is the average shear wave velocity in the top 30 metres below ground surface.

Table 2: Ground types - adapted from Eurocode 8 [30].

Ground type	Description of stratigraphic profile	$V_{s,30}$ $[m/s]$
A	Rock or other rock-like geological formation, including at most 5 m of weaker material at the surface.	> 800
B	Deposits of very dense sand, gravel, or very stiff clay, at least several tens of metres in thickness, characterised by a gradual increase of mechanical properties with depth.	$360 - 800$
C	Deep deposits of dense or medium dense sand, gravel or stiff clay with thickness from several tens to many hundreds of metres.	$180 - 360$
D	Deposits of loose-to-medium cohesionless soil (with or without some soft cohesive layers), or of predominantly soft-to-firm cohesive soil.	< 180
E	A soil profile consisting of a surface alluvium layer with V_s values of type C or D and thickness varying between about 5 m and 20 m, underlain by stiffer material with $V_s > 800\, m/s$.	
S_1	Depoosits consisting, or containing a layer at least 10 m thick, of soft clays/silts with a high plasticity index (PI > 40) and high water content.	< 100 (indicative)
S_2	Deposits of liquefiable soils, of sensitive clays, or any other soil profile not included in types A - E or S_1	

By application of this table and an appropriate choice of density and Poisson's ratio, the shear modulus of soil at a specific site can be estimated for the use in spring-dashpot representation of SSI.

2.1.3 Fluid System

Submerged structures exposed to dynamic loading will not only induce motions to the supporting soil, but also to the surrounding fluid - as the structure moves, it will push and pull on the fluid particles encompassing its structural elements.

A well-known empirical representation of this interaction is *Morison's equation* which was first proposed by Morison, O'Brien, Johnson and Schaaf in 1950 [28]. This equation describes the force exerted by surface waves on a cylindrical object, and it is composed of two force components; a *drag force* and a *virtual mass force*. In order to present this equation in a justified manner the two force components will be discussed firstly by looking at a cylindrical solid fully submerged in an incompressible fluid where the incident fluid velocity is perpendicular to the longitudinal axis of the cylindrical solid.

Fluid drag

Due to fluid viscosity, flow separation will occur behind a cylinder when subjected to an incident fluid flow. Differential pressure forces that oppose the motion of the cylinder, called form drag, will occur as shown in figure 5. Here, $\dot{u}_\mathrm{f}$ denotes the constant fluid velocity and q_D the drag force per unit length required to keep the cylinder stationary when subjected to the free stream fluid flow.

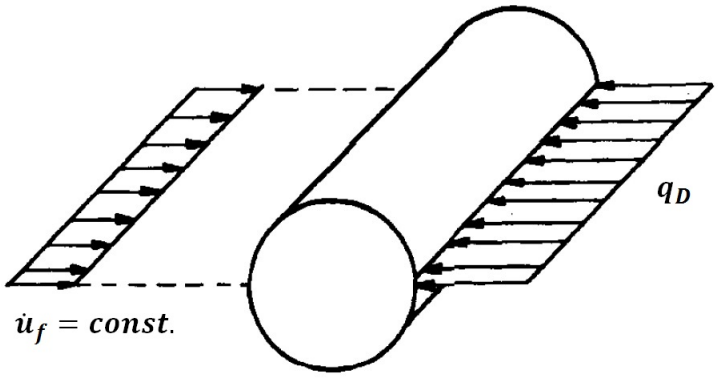

Figure 5: Stationary cylinder subjected to drag forces [37].

This drag force is proportional to the square of the flow velocity, $\dot{u}_\mathrm{f}$, and by measurements it is shown that it can be calculated using the following expression:

$$q_D = C_D \rho \frac{D}{2} |\dot{u}_\mathrm{f}| \dot{u}_\mathrm{f} \tag{2.1.14}$$

Here, ρ is the fluid density and D is the diameter of the cylindrical solid. The parameter C_D, called the coefficient of drag, is an important coefficient within the field of hydrodynamics. The drag coefficient largely depends on three factors which are the Reynolds number, Re, the Keulegan-Carpenter number, KC, and the roughness of the cylinder. These factors are used to characterize the fluid flow and a short description will be given here.

Faltinsen [21] describes four different flow regimes by the use of the Reynolds number as presented in table 3.

Table 3: Flow regimes defined by the Reynolds number [21].

Flow regime	Range
Subcritical flow	$Re <\approx 2 \cdot 10^5$
Critical flow	$\approx 2 \cdot 10^5 < Re <\approx 5 \cdot 10^5$
Supercritical flow	$\approx 5 \cdot 10^5 < Re <\approx 3 \cdot 10^6$
Transcritical flow	$\approx 3 \cdot 10^6 < Re$

The boundary layer in the subcritical flow is always laminar, and as the boundary layer grows, the viscous stresses will not be able to damp disturbances in the flow [17]. This will lead to a turbulent boundary layer upstream of the separation point in the supercritical and transcritical flow [21].

The drag coefficient, C_D, is approximately equal to unity for a smooth cylinder subjected to a constant free stream flow when the Reynolds number is within the range

$$10^3 \leq Re = \frac{\rho \dot{u}_\mathrm{f} D}{\mu} \leq 2 \cdot 10^5 \tag{2.1.15}$$

where μ is the viscosity of the fluid. In other words, $C_D \approx 1$, when the boundary layer is laminar by table 3.

The Keulegan-Carpenter number, KC, is a measure of how fast the fluid stream alternates [27]. It is given by

$$KC = \frac{u_0 T}{D} \tag{2.1.16}$$

where u_0 is the amplitude of the wave velocity and T is the wave period. With KC less than about 2, there is very little separation, and as the KC number increases separation will develop behind the cylinder, and the drag coefficient will increase by the definition of drag forces above. Literature on the subject gives different values of the limit values for KC with reference to separation, but in general the limit values lies within $1 \leq KC \leq 5$. It is worth noting that this transition to fully developed separation does not only depend on KC, but also on other factors [27].

The surface roughness of the cylinder is a ratio describing the average height of the surface roughness, k, to the diameter of the cylinder:

$$\text{surface roughness} = \frac{k}{D} \tag{2.1.17}$$

Due to marine growth the surface roughness in the North sea lies around a thickness of 10 cm down to 40 m below the mean water level, and for larger depths the thickness can be approximated by 5 cm [21].

To summarize, the drag coefficient, and hence the drag force on the cylinder, depends on a lot of factors and therefore it must be determined for each individual situation by assessing all relevant factors.

Fluid inertia

Whereas the drag force allow for real viscous fluid flow, the inertia force in Morison's equation does not - one assumes ideal, inviscid flow. The force per unit length required to hold a cylinder stationary when subjected to a constant, uniform free stream acceleration, $\ddot{u}_{\mathrm{f}}$, as shown in figure 6 is given by

$$q_I = C_M \rho \pi \frac{D^2}{4} \ddot{u}_{\mathrm{f}} \tag{2.1.18}$$

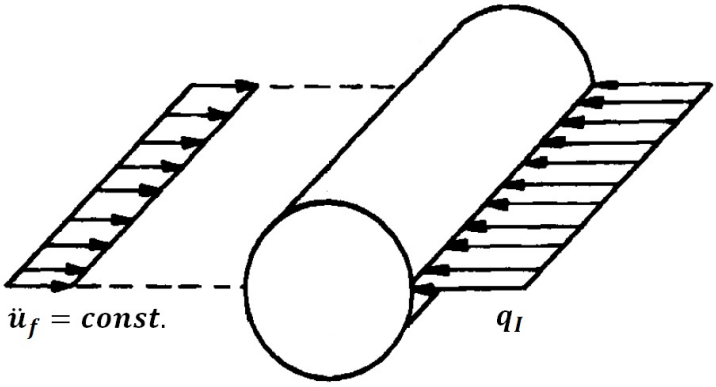

Figure 6: Stationary cylinder subjected to inertia forces [37].

The inertia coefficient, C_M, in equation 2.1.18 must in reality be empirically determined like the drag coefficient as it depends on the same parameters [21]. In relation to this coefficient, there is another coefficient known as the added mass coefficient, C_A:

$$C_A = C_M - 1 \tag{2.1.19}$$

A root-mean-square (rms) measured average of these to coefficients are usually used in applications, but for design purposes it is sufficient to use $C_A = 1$, and thereby, $C_M = 2$, if no such data exists and the length of the cylinder is much larger than its diameter.

Morison's Equation and Oscillatory Flow

By adding the drag and inertial forces described by equations 2.1.14 and 2.1.18 we end up with Morison's equation describing the load per unit length on the stationary cylinder in a plane flow field with a free stream velocity equal to $\dot{u}_\mathrm{f} = \dot{u}_\mathrm{f}(t)$:

$$q = C_D \rho \frac{D}{2} |\dot{u}_\mathrm{f}| \dot{u}_\mathrm{f} + C_M \rho \pi \frac{D^2}{4} \ddot{u}_\mathrm{f} \tag{2.1.20}$$

However, in relation to subsea earthquake engineering, it is of interest to look at the problem when the cylinder itself moves and not only when subjected to a steady current for instance as would be described by equation 2.1.20.

If the fluid is initially at rest, the force per unit length needed to give the cylinder an acceleration $\ddot{u}_\mathrm{c}$, is by Newton's second law of motion

$$q_\mathrm{I} = \left(m_0 + C_A \rho \pi \frac{D^2}{4} \right) \ddot{u}_\mathrm{c} = m \ddot{u}_\mathrm{c} \tag{2.1.21}$$

The expression in the parenthesis is a result of the fact that as the cylinder moves it will pull on the fluid particles around it. Thus, a virtual mass, m, is accelerated, which is made up of the actual cylinder mass per unit length, m_0, and the added or apparent mass $C_A \rho \pi D^2/4$.

Further, consider a simple cylinder-spring-dashpot system in a fluid initially at rest. If the cylinder is forced to vibrate, the fluid will be set in motion and then a relative velocity and acceleration will have to be introduced in equation 2.1.20. Thus, by combining equation 2.1.20 and 2.1.21, the resulting equation of motion becomes:

$$\left(m_0 + C_A \rho \pi \frac{D^2}{4} \right) \ddot{u}_\mathrm{c} + c \dot{u}_\mathrm{c} + k u_\mathrm{c} = C_D \rho \frac{D}{2} |\dot{u}_\mathrm{f} - \dot{u}_\mathrm{c}| (\dot{u}_\mathrm{f} - \dot{u}_\mathrm{c}) + C_M \rho \pi \frac{D^2}{4} (\ddot{u}_\mathrm{f} - \ddot{u}_\mathrm{c}) \tag{2.1.22}$$

where c is the structural damping per unit length, k is the structural stiffness per unit length and the remaining terms are defined by previous equations.

2.1.4 Interaction between systems

In real life, the foregoing systems do not act independently as presented, but behaves as a single system. For example, if we combine the first two systems, we can make some assumptions based on what is presented. Introducing springs and dashpots at the base of the structure gives reason to believe that the natural period of the system in the first mode for instance, T_1, will increase compared to that of a fixed base system. Although we may add stiffness and damping to the system, the fixed boundary conditions are removed, leading to a more flexible system. Assuming the reader is known with the eigenvalue problem of structural dynamics, reducing the stiffness and maintaining the mass will imply a reduced natural frequency, and thus an increased natural period.

Further, moving this "new" system from a dry environment to a wet environment introduces additional forces to consider. With drag and inertia forces in the picture, it is hard to say what the effect will become. Purely mathematically, as these forces depend on empirically determined coefficients, setting them equal to zero will render the same result as assumed in the foregoing paragraph. This is of course not consistent with reality as there *will be* drag and inertia forces. How much they will affect the system behaviour is really a question of the values assigned to these coefficients. However, following the same reasoning as above, the introduction of added mass, or more political correct, the added inertia, will lead to a lower natural frequency, and thus an even higher natural period.

Summarized, in the author's eyes there is reason to believe that the fully submerged structure will benefit in terms of structural demands from both SSI and the influence of the surrounding water when subjected to stong ground motions, compared to its response if it was situated onshore with a fixed base.

2.2 Earthquake Response Analysis

Within the field of earthquake engineering, the two main procedures used for estimating the response of a structure subjected to ground motion are *response history analysis* (RHA) and *response spectrum analysis* (RSA). The first procedure utilize the time variation, or history, of a ground acceleration, $\ddot{u}_g(t)$, to calculate the structural response as a function of time, whereas the latter procedure aims to predict the peak structural response when subjected to strong ground motion based on an earthquake response, or design, spectrum [15]. In this context, only the RHA will be presented through the concept of modal analysis, followed by a presentation of the numerical evaluation of the response. Section 2.2.1 is constructed based on theory provided by Chopra [15] and Villaverde [35], while theory in section 2.2.2 is taken from Cook [16] and lecture notes from a course on nonlinear finite element analysis lectured the fall of 2012 at NTNU [26].

2.2.1 Modal Analysis

Equation 2.1.5 represents a system of coupled equations. To make these equations uncoupled, that is making each of these equations depend on a single variable, modal analysis uses the orthogonality properties inherent in the mode shapes. These mode shapes and the corresponding frequencies are found by solving the eigenvalue problem.

The equation of motion for an undamped system under free vibration takes the form

$$\mathbf{M}\ddot{\mathbf{u}} + \mathbf{K}\mathbf{u} = 0 \tag{2.2.1}$$

The displacement, $\mathbf{u}$, can mathematically be described as a linear combination of the mode shapes, or equivalently, be transformed using

$$\mathbf{u}(t) = \mathbf{\Phi}\boldsymbol{\eta}(t) \tag{2.2.2}$$

where $\mathbf{\Phi}$ is the modal matrix containing the mode shapes, $\boldsymbol{\phi}_i$, and $\boldsymbol{\eta}(t)$ is a vector containing the unknown generalized, or normal, coordinates, $\eta_i(t)$, $i = 1, 2, ...N$. Letting the normal coordinates be simple harmonic functions and inserting them into equation 2.2.1 will yield

$$\mathbf{K}\boldsymbol{\phi}_i = \omega_i^2\mathbf{M}\boldsymbol{\phi}_i \tag{2.2.3}$$

as a trivial solution is uninteresting. This equation represents the matrix eigenvalue problem, and its solution will provide the N natural frequencies, ω_i, of vibration and the corresponding natural modes of vibration, $\boldsymbol{\phi}_i$. As mentioned initially, these mode shapes satisfy the following orthogonality conditions

$$\boldsymbol{\phi}_r^T \mathbf{M} \boldsymbol{\phi}_s = 0 \qquad r \neq s \tag{2.2.4a}$$

$$\boldsymbol{\phi}_r^T \mathbf{K} \boldsymbol{\phi}_s = 0 \qquad r \neq s \tag{2.2.4b}$$

Further by introducing this transformation of coordinates in equation 2.1.5 and premultiplying the equation by $\boldsymbol{\Phi}^T$ leads to

$$\boldsymbol{\Phi}^T \mathbf{M} \boldsymbol{\Phi} \ddot{\boldsymbol{\eta}}(t) + \boldsymbol{\Phi}^T \mathbf{C} \boldsymbol{\Phi} \dot{\boldsymbol{\eta}}(t) + \boldsymbol{\Phi}^T \mathbf{K} \boldsymbol{\Phi} \boldsymbol{\eta}(t) = -\boldsymbol{\Phi}^T \mathbf{M} \mathbf{L} \ddot{\mathbf{u}}_g(t) \tag{2.2.5}$$

By the orthogonality of the mode shapes, the triple matrix products $\boldsymbol{\Phi}^T \mathbf{M} \boldsymbol{\Phi}$, $\boldsymbol{\Phi}^T \mathbf{C} \boldsymbol{\Phi}$ and $\boldsymbol{\Phi}^T \mathbf{K} \boldsymbol{\Phi}$, now become the diagonal matrices, $\mathbf{M}^*$, $\mathbf{C}^*$ and $\mathbf{K}^*$, respectively, where the diagonal elements are scalars:

$$M_i^* = \boldsymbol{\phi}_i^T \mathbf{M} \boldsymbol{\phi}_i \qquad i = 1, 2, ...N \tag{2.2.6a}$$

$$C_i^* = \boldsymbol{\phi}_i^T \mathbf{C} \boldsymbol{\phi}_i \qquad i = 1, 2, ...N \tag{2.2.6b}$$

$$K_i^* = \boldsymbol{\phi}_i^T \mathbf{K} \boldsymbol{\phi}_i \qquad i = 1, 2, ...N \tag{2.2.6c}$$

These scalars are known as the *generalized mass*, the *generalized stiffness* and the *generalized damping constant*, respectively, of the system in its ith mode of vibration. By denoting the triple matrix product $\boldsymbol{\Phi}^T \mathbf{M} \mathbf{L} = \mathbf{P}^*$ we now get the following equations of motion:

$$\mathbf{M}^* \ddot{\boldsymbol{\eta}} + \mathbf{C}^* \dot{\boldsymbol{\eta}} + \mathbf{K}^* \boldsymbol{\eta} = -\mathbf{P}^* \ddot{\mathbf{u}}_g(t) \tag{2.2.7}$$

This equation may be considered as a system of equations of motion for N single-degree-of-freedom systems with mass M_i^*, stiffness K_i^* and damping constant C_i^*:

$$M_i^* \ddot{\eta}_i + C_i^* \dot{\eta}_i + K_i^* \eta_i = -P_i^* \ddot{u}_g(t) \qquad i = 1, 2, ..., N \tag{2.2.8}$$

Dividing 2.2.8 by the generalized mass renders

$$\ddot{\eta}_i + 2\xi_i \omega_i \dot{\eta}_i + \omega_i^2 \eta_i = -\Gamma_i \ddot{u}_g(t) \qquad i = 1, 2, ..., N \tag{2.2.9}$$

Here, the undamped natural frequency, ω_i, is equal to

$$\omega_i = \sqrt{\frac{K_i^*}{M_i^*}} \tag{2.2.10}$$

and the damping ratio, ξ_i, is equal to

$$\xi_i = \frac{C_i^*}{2\omega_i M_i^*} \tag{2.2.11}$$

The participation factor, Γ_i, scales the ground motion for each mode and thereby is a measure of how much the mode contributes to the response, and is defined as the ratio

$$\Gamma_i = \frac{\boldsymbol{\Phi}_i^T \mathbf{M} \mathbf{L}}{\boldsymbol{\phi}_i^T \mathbf{M} \boldsymbol{\phi}_i} \tag{2.2.12}$$

The Duhamel integral may be used to solve equation 2.2.9:

$$\eta_i(t) = \frac{\Gamma_i}{\omega_{D,i}} \int_0^t \ddot{u}_g(\tau) e^{-\xi_i \omega_i (t-\tau)} \sin \omega_{D,i}(t-\tau) d\tau \tag{2.2.13}$$

where the damped natural frequency of the system in its ith mode is given as $\omega_{D,i} = \omega_i(1-\xi_i^2)^{1/2}$. Equation 2.2.13 may also be expressed as

$$\eta_i(t) = \Gamma_i z_i(t) \tag{2.2.14}$$

where $z_i(t)$ is the relative displacement response.

With the generalized coordinates determined, the displacement of the structure may be calculated by

$$\mathbf{u}(t) = \sum_{i=1}^{N} \boldsymbol{\phi}_i \eta_i(t) = \sum_{i=1}^{N} \Gamma_i \boldsymbol{\phi}_i z_i(t) \tag{2.2.15}$$

and the response problem is in large degree determined as the velocities, accelerations and internal forces of the system are derived from the displacements.

Comment on Damping

Damping is a term used for the process by which the amplitude of the free vibration diminishes with time. It can be inherent, or it can be added to limit the peak response, and in relation to structural dynamics the following forms of damping are significant

- Viscous damping.
- Hysteresis damping, or solid damping.
- Coulomb damping.
- Radiation damping.

In addition, there is also the possibility of introducing algorithmic damping, or numerical dissipation, when using direct time integration methods. Usually, the damping forces in a structural dynamics problem are considered to be less than 10 % of the other forces

given in the equation of motion, and it is therefore most often sufficient to model it as viscous damping, regardless of its actual source [16].

A common way to represent this viscous damping is by the use of Rayleigh damping. Here the damping matrix, $\mathbf{C}$, is constructed as a linear combination of the mass and stiffness matrices by

$$\mathbf{C} = \alpha\mathbf{M} + \beta\mathbf{K} \tag{2.2.16}$$

Inspecting a sdof system yields a damping ratio equal to

$$\xi = \frac{1}{2}\left(\frac{\alpha}{\omega} + \beta\omega\right) \tag{2.2.17}$$

As shown in figure 7 the coefficients in 2.2.16 are determined by choosing a frequency range and assigning appropriate damping ratios to the extremities of this range:

$$\alpha = 2\omega_1\omega_2\frac{\xi_1\omega_2 - \xi_2\omega_1}{\omega_2^2 - \omega_1^2} \tag{2.2.18a}$$

$$\beta = 2\frac{\xi_2\omega_2 - \xi_1\omega_1}{\omega_2^2 - \omega_1^2} \tag{2.2.18b}$$

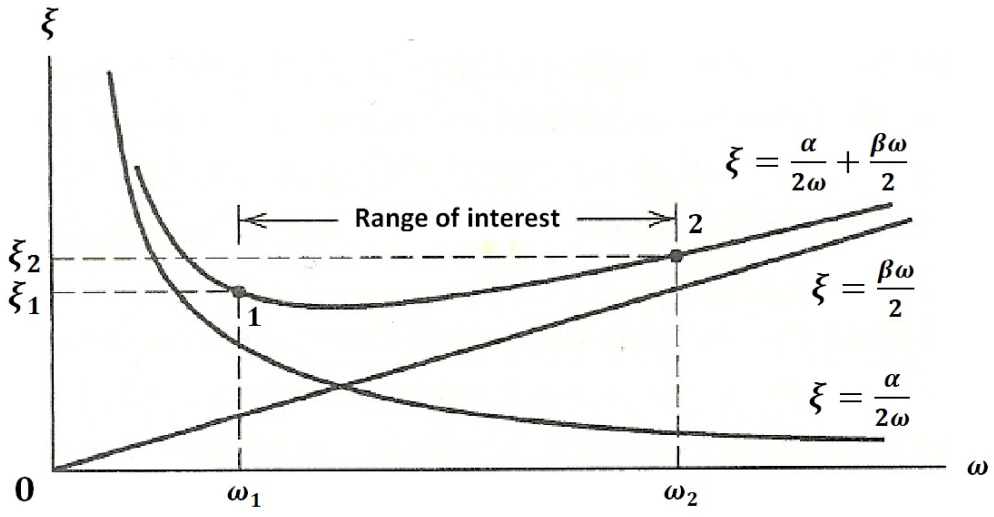

Figure 7: Fraction of proportional damping [16].

Also, figure 7 illustrates that the lowest modes are damped mainly by the mass proportional term, $\alpha\mathbf{M}$, whereas the higher modes are damped most heavily by the stiffness proportional term, $\beta\mathbf{K}$ [16].

2.2.2 Numerical Response

For systems with nonclassical damping, or if the system responds into the nonlinear range, uncoupling of the modal equations is not possible. In such problems the equation of motion must be numerically evaluated by choosing an appropriate algorithm, rather than solving the problem analytically [15]. The finite element method is a powerful tool in analysing complex problems, and in this context the numerical schemes will be presented in a finite element format and related to the software used in this thesis, Abaqus.

Provided a time series of either acceleration, velocity or displacement is given the response history may be calculated using step-by-step integration in time, also known as direct integration, of the dynamic equations without altering them as is done in modal analyses.

Denoting the time step Δt, the equilibrium equation in the ith time step in a general structural dynamics problem is given by

$$\mathbf{M}\ddot{\mathbf{u}}_i + \mathbf{C}\dot{\mathbf{u}}_i + \mathbf{R}_i^{\text{int}} = \mathbf{R}_i^{\text{ext}} \tag{2.2.19}$$

where $\ddot{\mathbf{u}}_i$ and $\dot{\mathbf{u}}_i$ are the nodal accelerations and velocities, $\mathbf{M}$ and $\mathbf{C}$ are the mass and damping matrices, and $\mathbf{R}_i^{\text{int}}$ and $\mathbf{R}_i^{\text{ext}}$ are the internal and external force vectors, respectively.

The response history and thereby equation 2.2.19 can either be solved by an explicit or an implicit integration scheme. In explicit methods the displacement at time t_{i+1}, $\mathbf{u}_{i+1}$, is obtained directly from previous equilibrium conditions at one or more preceding time steps $t \leq t_i$. Hence, there is no need for solving an equation system. Implicit methods on the other hand require equation solving as the displacement $\mathbf{u}_{i+1}$ are obtained indirectly from the equilibrium conditions at time t_{i+1}. Further, the explicit methods are only conditionally stable, that is they require very small time steps, whereas the implicit methods are for linear problems unconditially stable, meaning there is no restriction on the time increment size, and thus fewer increments are required. For the purpose of this thesis an implicit scheme will in the following be assumed due to its advantage of unlimited increment size, as the time series used herein spans from 0 to about 30 seconds meaning an explicit scheme would probably be more computationally expensive.

For a system subjected to strong ground motions as is the case for this thesis, the total acceleration in equation 2.2.19 will be equal to the sum of the relative accelerations $\ddot{\mathbf{u}}_i$ and the ground accelerations $\ddot{\mathbf{u}}_{g,i}$. Further, the internal force vector, $\mathbf{R}_i^{\text{int}}$ will for linear problems be equal to

$$\mathbf{R}_i^{\text{int}} = \mathbf{K}\mathbf{u}_i \tag{2.2.20}$$

However, for nonlinear problems, the principle of superposition does not apply and the stiffness and perhaps load vector may be functions of the displacement. For example, the Newton-Raphson method operates with what is called the tangent stiffness,

$$\mathbf{K}_{T,n} = \left(\frac{\partial \mathbf{R}^{\text{int}}}{\partial \mathbf{u}} \right)_n \tag{2.2.21}$$

Thus, for an applied load $\mathbf{F}_1$, it is necessary to iterate in order to find the corresponding displacement, $\mathbf{u}_1$. This means, the system stiffness will have to be updated for each time increment. Denoting n the total number of iterations per increment, and including eventual external loads F, equation 2.2.19 for a system subjected to strong ground motions may be written as:

$$\mathbf{M}\ddot{\mathbf{u}}_i + \mathbf{C}\dot{\mathbf{u}}_i + (\mathbf{K}\mathbf{u})_i^n = \mathbf{F}_i - \mathbf{M}\ddot{\mathbf{u}}_{g,i} \tag{2.2.22}$$

A well known direct, implicit integration procedure is that of Newmark's method. In many problems it is of interest to introduce dissipation of high-frequency modes as the response of these modes often are of little interest, or, because they only amount to noise. To damp this noise, it is preferable to employ algorithmic damping, and this is for the Newmark method done by setting the parameter $\gamma > 0.5$. The drawback by introducing this numerical damping is that the accuracy of the solution will be reduced from second-order to first-order.

However, another implicit integration scheme exists which is more effective in damping high-frequency modes, as well as maintaining second order accuracy. This is the method of Hilber, Hughes and Taylor, abbreviated to the HHT α-method, and it is the method applied in this thesis. This method is based on the same finite difference formulas as those utilized in the Newmark method:

$$\dot{\mathbf{u}}_{i+1} = \dot{\mathbf{u}}_i + \Delta t \left[\gamma \ddot{\mathbf{u}}_{i+1} + (1-\gamma)\ddot{\mathbf{u}}_i \right] \tag{2.2.23a}$$

$$\mathbf{u}_{i+1} = \mathbf{u}_i + \Delta t \dot{\mathbf{u}}_i + \frac{1}{2}\Delta t^2 \left[2\beta \ddot{\mathbf{u}}_{i+1} + (1-2\beta)\ddot{\mathbf{u}}_i \right] \tag{2.2.23b}$$

The time-discrete equation of motion now becomes:

$$\mathbf{M}\ddot{\mathbf{u}}_{i+1} + (1+\alpha_H)\mathbf{C}\dot{\mathbf{u}}_{i+1} - \alpha_H \mathbf{C}\dot{\mathbf{u}}_i + (1+\alpha_H)\mathbf{K}\mathbf{u}_{i+1} - \alpha_H \mathbf{K}\mathbf{u}_i = \mathbf{R}_\alpha^{\text{ext}} \tag{2.2.24}$$

Here $\mathbf{R}_\alpha^{\text{ext}} = (1+\alpha)\mathbf{R}_{i+1}^{\text{ext}} - \alpha_H \mathbf{R}_i^{\text{ext}}$ is the external load vector evaluated at time $t_{i+1} + \alpha_H \Delta t$. The parameter α_H is used to introduce algorithmic damping by assigning it a value < 0, and the method is unconditionally stable when this parameter lies within the range $[-\frac{1}{3}, 0]$.

3 Earthquake excitation

The simulation method utilized in this thesis is meant to be of a more generalized character rather than site-specific. In order to produce earthquake excitations, predefined geographical source zones of polygonal shape are used as shown in figure 8. This figure shows the zones adapted from [4], which are used in the simulation. Within each of these zones the epicentres are assumed uniformly distributed, and furthermore, the Gutenberg-Richter parameters and lower and upper bounds of magnitude are assumed constant.

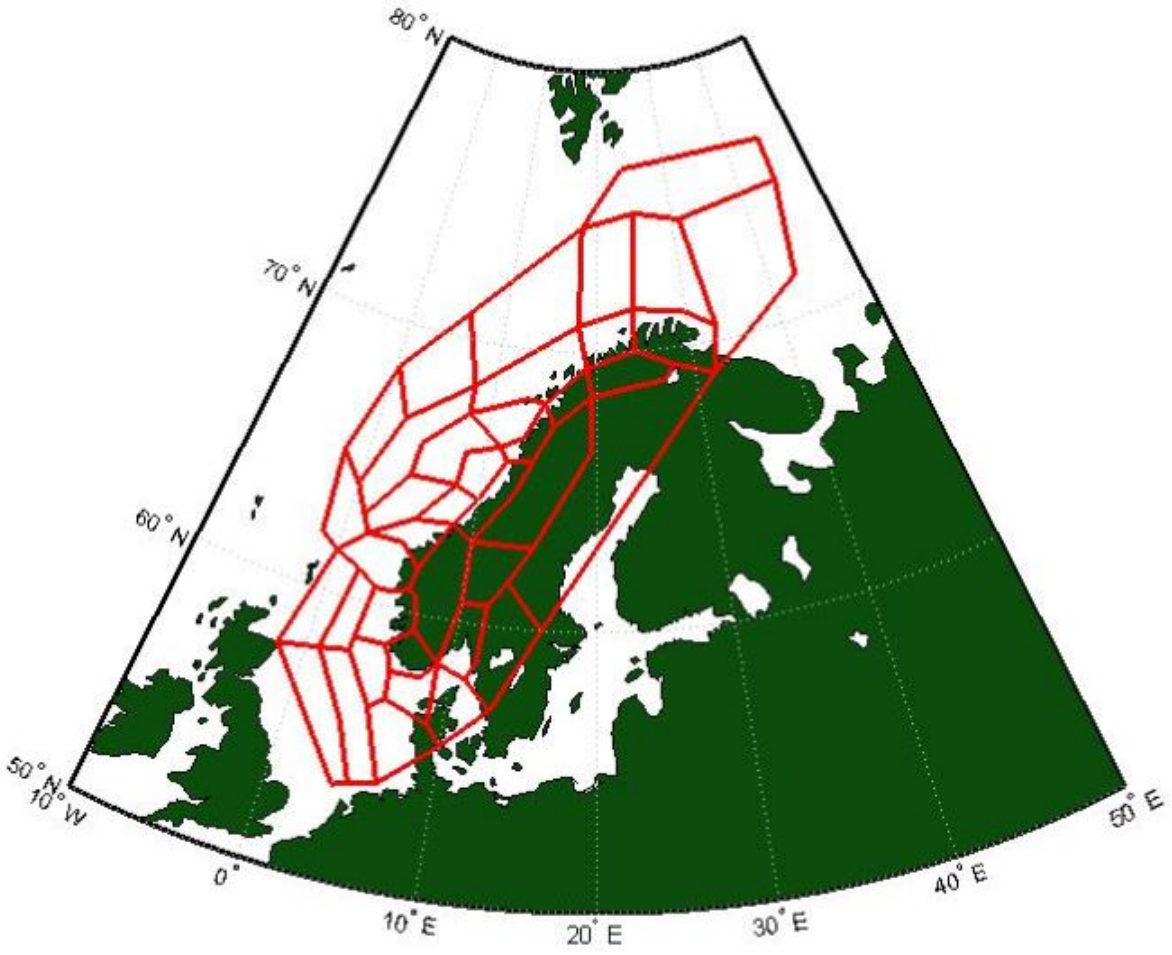

Figure 8: Seismic source zones created based on zones provided in [4].

To obtain the earthquake excitation the following main steps are carried out:

1. Generation of synthetic earthquake catalogue with input data from the assumed source zone map.
2. Derivation of the desired ground motion quantity for the prescribed location of the structure of interest by application of an appropriate ground motion prediction model.

3. Derivation of the extreme value distribution of the ground motion quantity by use of order statistics; the design ground motion is computed for a prescribed return period to obtain the event that is contributing most to the ground motion and the earthquake response for this particular return period.

The outcome of this procedure is an event defined by epicentral distance and magnitude which is assumed to contribute most to the response for a given return period. Using these data a proper time series can be selected from a database of strong ground motions and further on be used in the structural response analysis.

3.1 Generation of synthetic earthquake catalogue

The Matlab script "EarthquakeCatalogue.m" [33] generates an earthquake catalogue with randomly spaced earthquakes of random size and character restricted by respective prescribed bounds. The algorithm utilized in this script is described below.

Firstly, the number of earthquakes and their respective magnitudes are created for each source zone in accordance with the Gutenberg-Richter law [25] defined as follows:

$$\ln N = \alpha - \beta M \tag{3.1.1}$$

Here, α and β are parameters defined for each source zone describing the overall seismicity which in this case study, were extracted from a report on seismic zonation for Norway [4]. Furthermore, an upper and lower bound on magnitude value is defined for each source zone, M_{min} and M_{max}. By the information given in the zonation report [4], these were assigned values of 4 and 6.4, respectively. The number of earthquakes simulated for each source zone is determined by the following derivative of equation 3.1.1:

$$N = \frac{e^{\alpha}}{\beta}\left(e^{-\beta M_{min}} - e^{-\beta M_{max}}\right) \tag{3.1.2}$$

And the corresponding vector of magnitudes is computed by following derivative from equation 3.1.1:

$$M = M_{min} - \frac{1}{\beta}\ln\left(1 - x\left(1 - e^{-\beta(M_{max} - M_{min})}\right)\right) \tag{3.1.3}$$

where x is a vector of random numbers uniformly distributed between 0 and 1.

Secondly, the location of the uniformly distributed epicentres is computed. The output of equation 3.1.2 is multiplied by a factor of ten to create a sufficient amount of events randomly located within a rectangular area defined by the maximum and minimum coordinates of the polygonal shaped area. Further, the epicentres located within the polygonal shaped source zone are extracted and, if necessary, corrected downwards towards the number of epicentres given by equation 3.1.2.

Finally, the faulting mechanism is generated. The style of faulting is assumed uniform within each source zone and is randomly chosen from one of the three scenarios if there is no specific data on the subject to be found; normal faulting, thrust faulting or odd faulting.

The above outlined procedure is repeated for each source zone on the zonation map. The output data for each source zone is then stored in a data structure which contains the needed information regarding the spatial structure of an earthquake catalogue. The temporal structure on the other hand is missing which does not disturb the following applications.

3.1.1 Comment

In the zonation report, there is some uncertainty connected to the seismicity parameters, α and β. The report presents two zonation maps, where the β-value for all zones is set equal to 1.05. One map is constructed based on the zonation done during the GSHAP project, whereas the other is new of this study. The α-values for these two maps is constructed based on an additional large zone map where $\alpha = 4.32$ - the α-values are normalized to this "target-value". Furthermore, each of these values are presented with a set of weights which are not really explained regarding how they are found, or possibly how they should be used with the given α-values. Therefore, the zonation parameters related to the map "new" of this study are employed as they are, whereas the question of this is correct or not will be left for further studies.

3.2 Ground motion quantities

The ground motion quantity to be applied in the following is the peak ground acceleration (PGA). The following model is considered in the present study [6] [7]

$$\log PGA = a_1 + a_2 M + (a_3 + a_4 M) \log \sqrt{d^2 + a_5^2} + a_6 S_S + a_7 S_A + a_8 F_N + a_9 F_T + a_{10} F_O + \epsilon \tag{3.2.1}$$

Here, M denotes moment magnitude, d denotes the distance between the epicentre and the site of interest, a_i, $i = 1, \cdots, 10$, are constants found by regression analysis found in table 4, S_i, $i = (S, A)$, is the characterization of the soil at the site; $S_S = 1$ for soft soil sites and 0 otherwise, $S_A = 1$ for stiff soil sites and 0 otherwise, F_i, $i = (N, T, O)$, is the characterization of the faulting style; $F_N = 1$ for normal faulting earthquakes and 0 otherwise, $F_T = 1$ for thrust faulting earthquakes and 0 otherwise and $F_O = 1$ for odd faulting earthquakes and 0 otherwise, and ϵ is a random error term.

The random error term, ϵ, is the residual resulting from the difference between the ground motion observation and its predicted value, it says something about the scatter in the data. It has a mean of zero and a standard deviation equal to the standard error of

Table 4: Constants used in attenuation model extracted from the articles by Ambraseys et. al. [6] and [7].

Coefficient	Horizontal PGA	Vertical PGA
a_1	2.5220	0.8350
a_2	-0.1420	0.0830
a_3	-3.1840	-2.4890
a_4	0.3140	0.2060
a_5	7.6000	5.6000
a_6	0.1370	0.0780
a_7	0.0500	0.0460
a_8	-0.0840	-0.1260
a_9	0.0620	0.0050
a_{10}	-0.0440	-0.0820
Standard deviation		
σ_1	$0.665 - 0.065M$	0.262
σ_2	$0.222 - 0.022M$	0.100

estimate of $\ln PGA$, $\sigma_{\ln PGA}$. This standard deviation can be looked upon as a combination of an intra- or within-earthquake standard deviation, σ_1, and an inter- or between-earthquake standard deviation, σ_2 [14];

$$\sigma_{\ln PGA} = \sqrt{\sigma_1^2 + \sigma_2^2} \tag{3.2.2}$$

The values of these components of the standard deviation of the error are given in the lower part of table 4, and figure 9 gives a graphical description of the total standard deviation:

More specifically, the intra-earthquake standard deviation refers to so called intra-event terms (individual recordings), whereas the inter-earthquake standard deviation refers to terms common to all recordings of a specific earthquake, so-called inter-event terms [12]. For this study the random error term is computed by

$$\epsilon = n \cdot \sigma_2 \tag{3.2.3}$$

where n is a random number within the range $[0, 1]$.

The only inputs needed for the model described by equation 3.2.1 are the earthquake moment magnitudes and epicentral distances obtained from the synthetic earthquake catalogue introduced in section 3.1. The distances between the epicentres and the site of

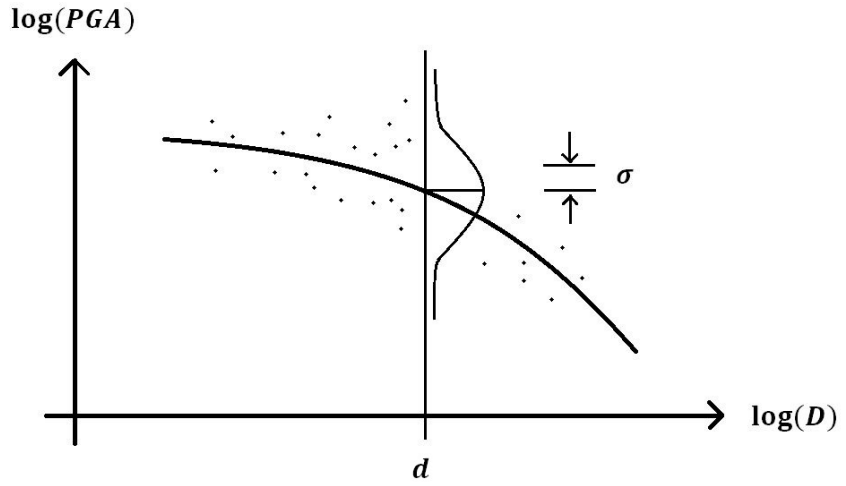

Figure 9: Graphical representation of the standard deviation of the residual.

interest are approximated by the following equation in order to account for the fact that the earth is round and not flat:

$$d = 111\sqrt{(N - Ne)^2 + \left((W - We) \cdot \cos\left(\frac{\pi\,(N - Ne)}{2 \cdot 180}\right)\right)^2} \tag{3.2.4}$$

Here, the epicentre coordinates are denoted Ne and We for latitude and longitude, respectively, and the coordinates of the site of interest are denoted N and W for latitude and longitude, respectively [32].

The ground motion regression model presented here has an inherent uncertainty to it as it to some degree is constructed based on subjectivity, and it is important to recognize that this is a model giving an estimate of the ground motion rather than an exact prediction. For example, the process of determining which earthquakes to include and which to exclude is important as the reliability of the coefficients depends on the underlying data set. Another example is the appropriate choice of cut-off frequencies in relation to filtering of strong-motion records, where some subjectivity was involved in the process [6] [7].

3.3 Order statistics, extremes and de-aggregation

In order to find a representative earthquake for a given return period, order statistics is performed on the ground motion quantities obtained in section 3.2. The basic assumptions made are that the generated earthquakes are independent and identically distributed within each source zone. This does not correspond to reality as the location and magnitude of earthquakes depend on local geological conditions, for instance if the location is close to a fault or to the Mid-Atlantic Ridge in this case, there is higher seismic activity here than further away. In reality the conditions are not stationary, whereas this is a necessary assumption for the generation of the earthquake catalogue as the time span of the available data on earthquake recurrence is limited.

To fit a proper extreme value distribution to the simulated data, the results are plotted as shown in figure 10. The model employed in this study is that of the Gumbel distribution for maxima with reference to the appendix, section A. Its cumulative distribution function (cdf) is given as follows:

$$F(t) = P(X \leq x) = e^{-e^{-x}} \tag{3.3.1}$$

Taking natural logarithms twice of equation 3.3.1 gives a linear relation in in x_i, here replaced by PGA_i, given by:

$$-\ln\left(-\ln\left(F(PGA_i)\right)\right) = PGA_i \tag{3.3.2}$$

Further replacing $F(PGA_i)$ by a suitable plotting position p_i gives

$$y = -\ln\left(-\ln\left(p_i\right)\right) = c_1 + c_2 PGA_i \tag{3.3.3}$$

The plotting position used in this thesis is the one provided by Gringorten [13]:

$$p_i = \frac{i - 0.44}{n + 0.12} \tag{3.3.4}$$

By computing the plotting positions for each PGA value extracted from the earthquake catalogue, the regression parameters c_1 and c_2 can be obtained and the regression line for the specified fraction of the tail is determined.

Further, for the mean return period we have:

$$P(R) = \frac{1}{R} \tag{3.3.5}$$

where R is the return period, and taking natural logs twice again of the cdf given in equation 3.3.1 gives the following relation for the assigned return period:

$$-\ln\left(-\ln\left(\frac{1}{R}\right)\right) = y\left(R\right) \tag{3.3.6}$$

The result of this is that the response quantity, PGA, for a given return period, R, can be computed from

$$\begin{aligned} PGA_R &= \frac{-\ln(-\ln(1-P(R)) - c_1}{c_2} \\ &= \frac{-\ln\left(-\ln\left(1-\frac{1}{R}\right)\right) - c_1}{c_2} \end{aligned} \tag{3.3.7}$$

Figure 10 summarizes the procedure presented in this section. It is an example of the horizontal PGA corresponding to a return period of 10 000 years, and as can be seen, within the confidence limits, $PGA_{10000} \approx 3\ m/s^2$.

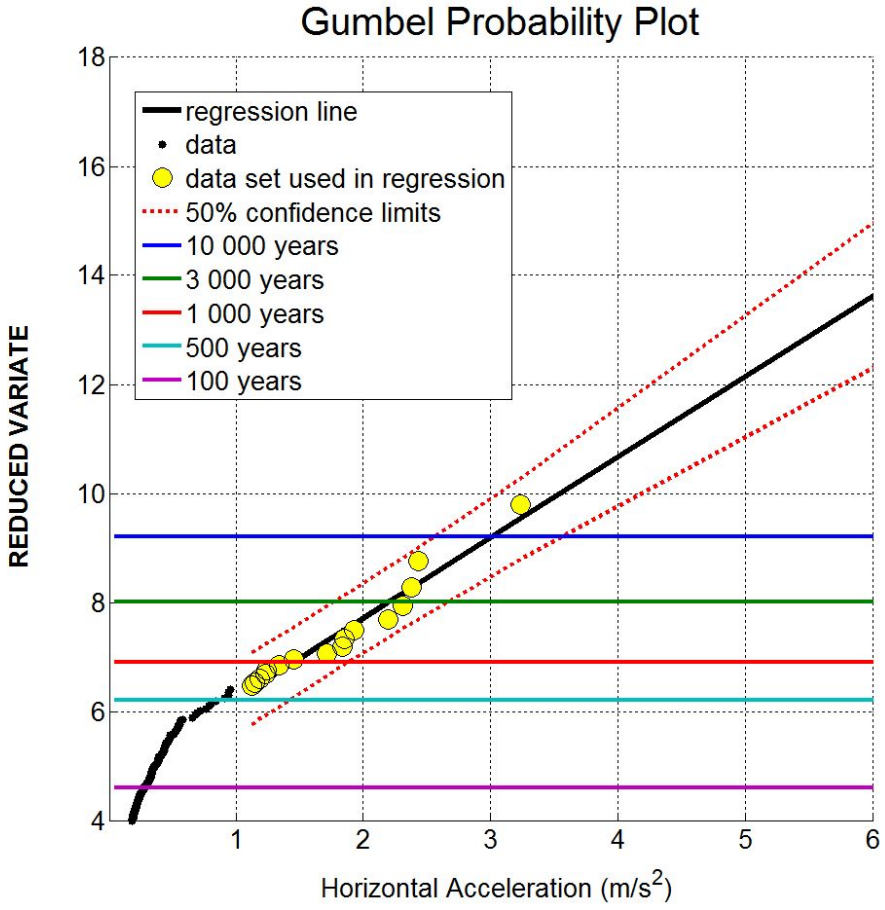

Figure 10: Gumbel probability plot of the horizontal PGA for a return period of 10 000 years. Site: The Halten Terrace.

3.4 Acceleration time series

With the calculated peak ground accelerations in both horizontal and vertical direction using extreme value distribution and de-aggregation, it is possible to find an appropriate acceleration time series using *Dissemination of European Strong-Motion Data, Vol. 2* (ESMD). This is a CD ROM containing corrected acceleration, velocity and displacement records and additional data of 462 triaxial strong-motion records originating from 110 earthquakes in Europe and the Middle East [5].

Two sites offshore Norway are considered in this thesis. The first site, the Åsgård field located on the Halten Terrace, is chosen because this is the site where the study case of this thesis is located. The second site is chosen to be the Statfjord field due to its high seismic activity (in Norwegian scale) measured by its seismicity parameters [4]. The two locations are shown in figure 11 showing the southern and mid part of Norway [22]. Due to computational cost, the time histories presented here are scaled, that is, the recordings span over a longer period of time but are shortened by selecting appropriate minimum values of acceleration, for example $PGA > 0.3$.

Figure 11: The offshore sites considered in this thesis [22].

3.4.1 The Åsgård Field

Considering a return period of 10 000 years, the results for the Halten Terrace render a horizontal PGA, PGA_H and a vertical PGA, PGA_V, equal to

$$PGA_H = 3.23\, m/s^2$$

$$PGA_V = 2.57\, m/s^2$$

In the ESMD an earthquake recorded on South Iceland with $PGA = 3.3408$, is chosen, and the corresponding acceleration time series are shown in figure 12 below.

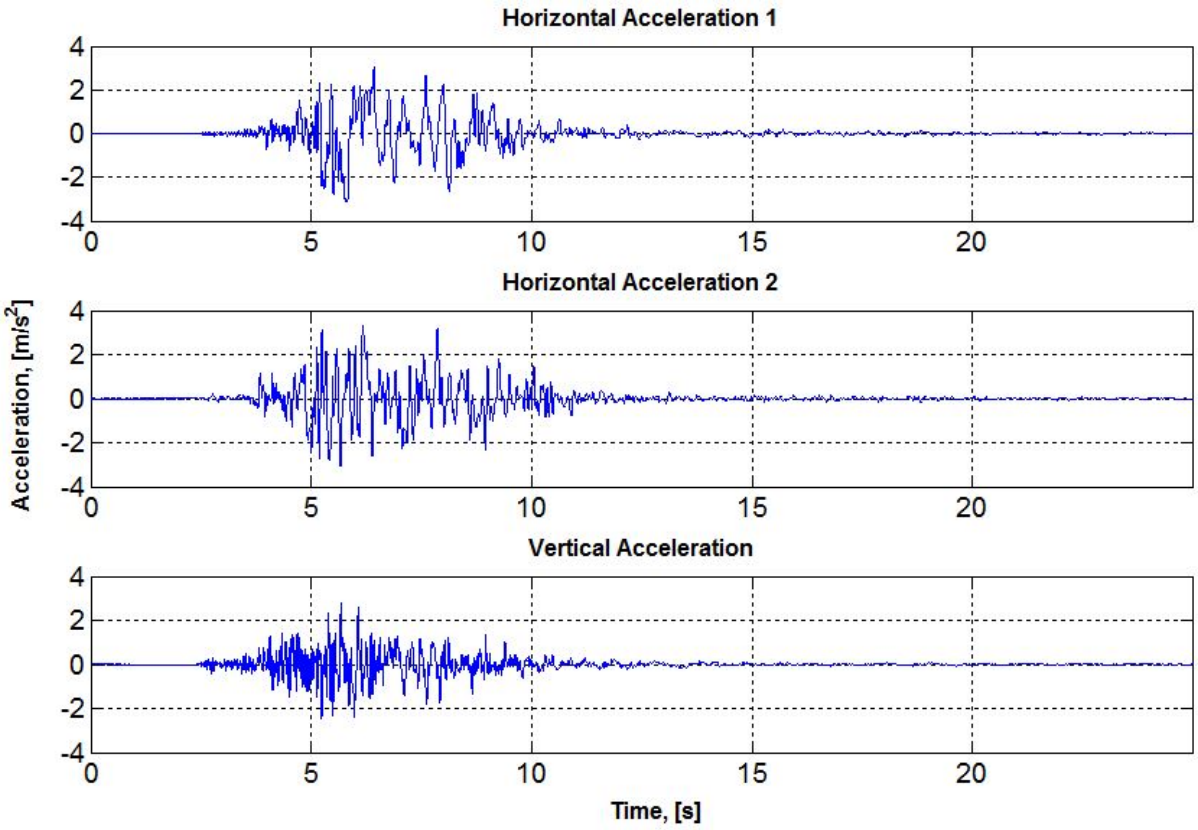

Figure 12: Acceleration time histories used for the Åsgård field.

3.4.2 The Statfjord Field

The peak ground accelerations corresponding to a return period of 10 000 years for the Statfjord field was found to be

$$PGA_H = 4.05\, m/s^2$$

$$PGA_V = 1.43\, m/s^2$$

A search in the ESMD resulted in three recordings from the Friuli earthquake which occurred in 1976. The PGA of these recordings are equal to 4.1003 occuring in the second horizontal acceleration time series as shown in figure 13.

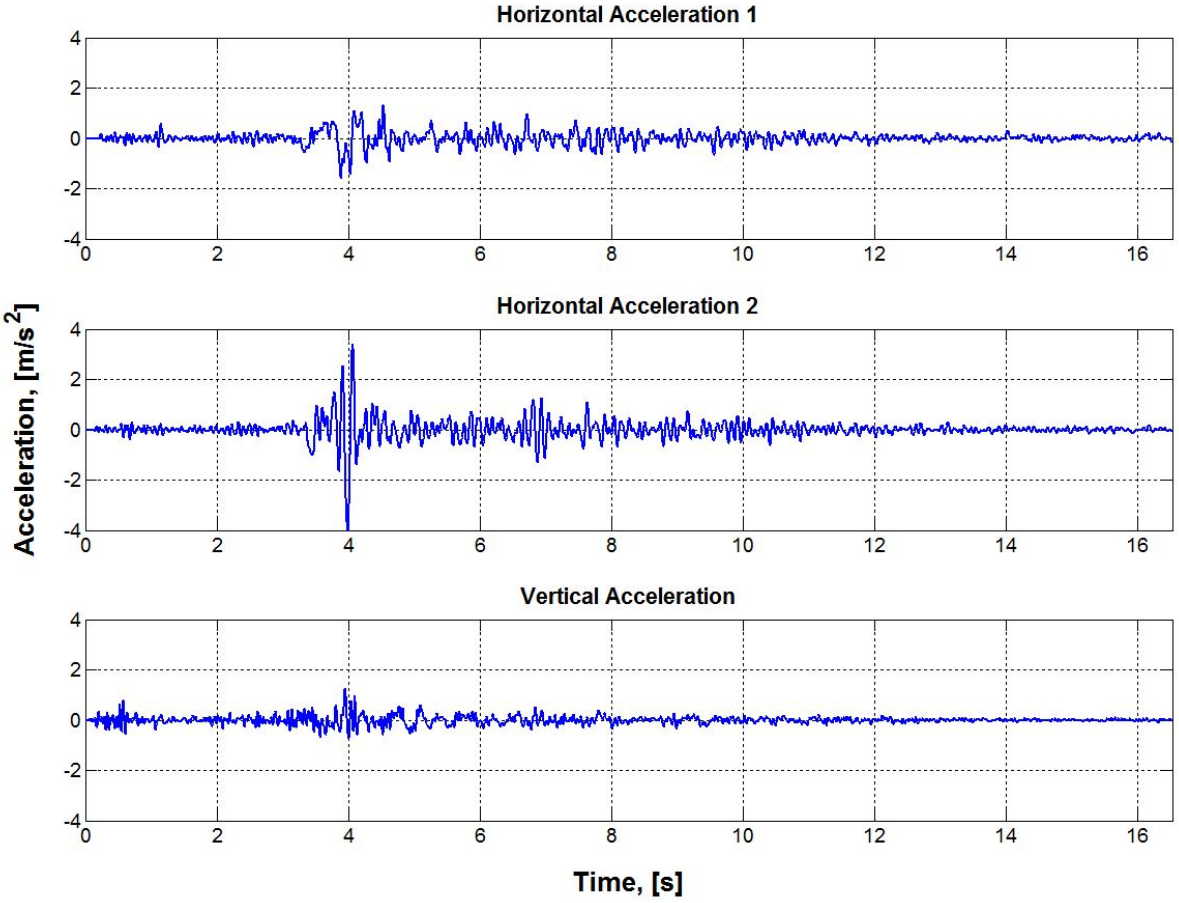

Figure 13: Acceleration time histories used for the Statfjord field.

4 Case study

4.1 Definition of the Case

The construction chosen as the study case for this thesis is that of a protection structure. The structure is more commonly known as "Hot-Tap-Tee Protection Structure (HTT PS)", and its geometry and other specifications are provided by Reinertsen AS [2]. A picture of the structure under construction is shown in figure 14.

Figure 14: Photo of the HTT PS during construction [2].

The structure is located at the Åsgård field on the Halten Terrace at a depth of approximately 270 m below sea level in relation with Norwegian oil production. Similar protection structures are commonly used on the entire Norwegian continental shelf, however the function of these structures is not directly related to the oil production, but rather to the fishing industry. As there is a risk for objects dropping down and hitting the various installations at the seabed, the protection structure prevents damages to these installations if such events should occur. In oil fields located at shallow water depths there is also the danger of a trawl damaging the the oil installations, which constitutes that the protection structures are important structures with reference to eventual events that would cause damage if the structure was not there.

4.1.1 Geometry and Material

Compared to the vast amount of human made constructions both above and below sea level the HTT PS is a small construction. It weighs about 60 tons and it is approximately 7 meters high and covers a an area of 19x22 meters squared at its base as shown in figure 15.

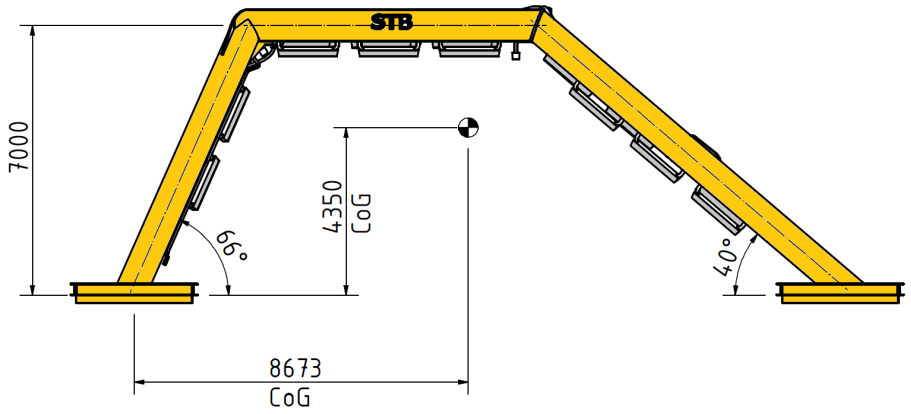

(a) Side view of the HTT PS.

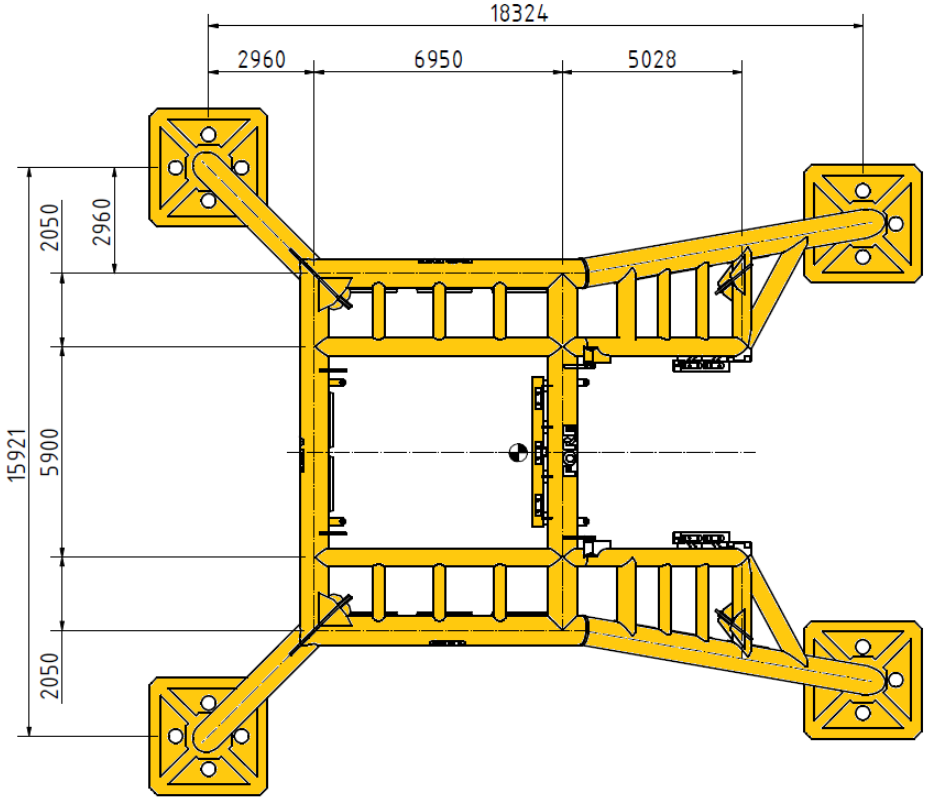

(b) Top view of the HTT PS.

Figure 15: Global dimensions of the HTT PS [2].

Figure 14 and figure 16 shows that the main components of the structure are beams, two hatches and four pads. The beams all have pipe cross-sections whereas the pads are roughly made up of six HE300B beams per pad and short skirts. The dimensions of the main members are shown in table 5, whereas the dimensions of the components in the hatches are not given in the provided construction drawings. The material used in the main components are steel with a Young's modulus of $E = 2.1 \cdot 10^5$ MPa, a Poisson's ratio of $\nu = 0.3$, quality S355 and a density of $\rho_s = 7850 kg/m^3$ [2].

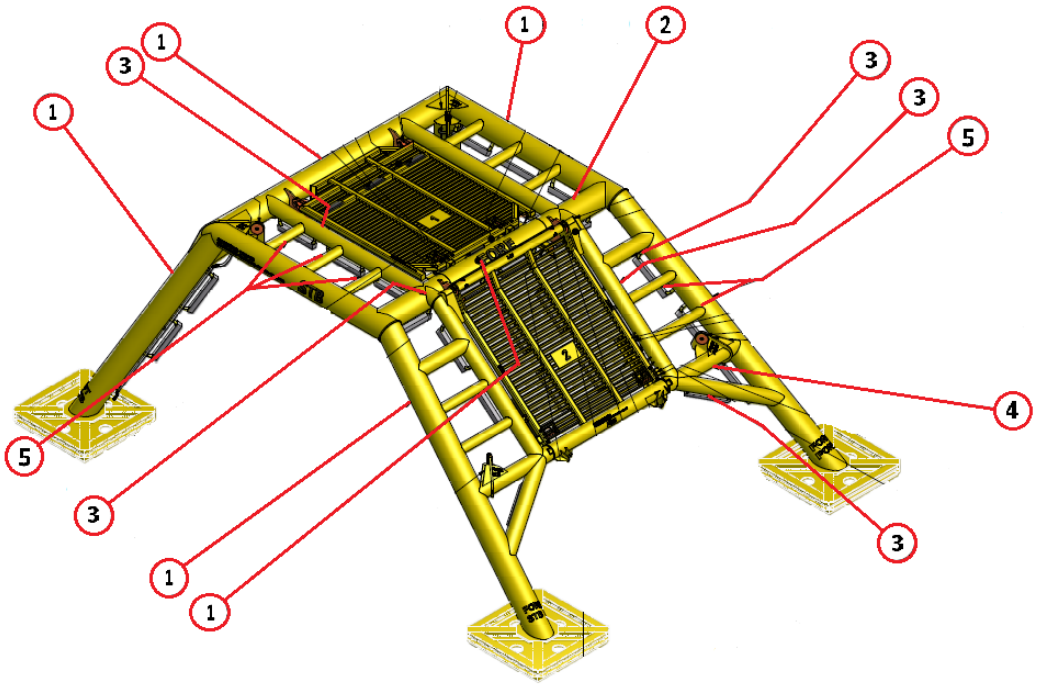

Figure 16: The main structural members of the HTT PS [2].

Table 5: Dimensions of the main structural members [2].

Main structural member	Profile [mm]
1	CHS 813.0x20.0
2	CHS 813.0x30.0
3	CHS 508.0x12.0
4	CHS 508.0x30.0
5	CHS 323.9x10.0

4.1.2 The Foundation

Figure 17 gives a graphical illustration of the HTT PS in its real environment. The soil conditions at the Halten Terrace are assumed to largely be represented by soft clay, but as can be seen from the figure the foundation of the HTT PS is made up of rock. Whether the rock covers the pads entirely or not varies, but as the soil is assumed to be of soft clay it is necessary to provide some solid ground for constructions with shallow foundations like in this case. Also, the members of the structure are filled with water, which is an important factor with regards to dynamic modelling of the structure due to added mass effects.

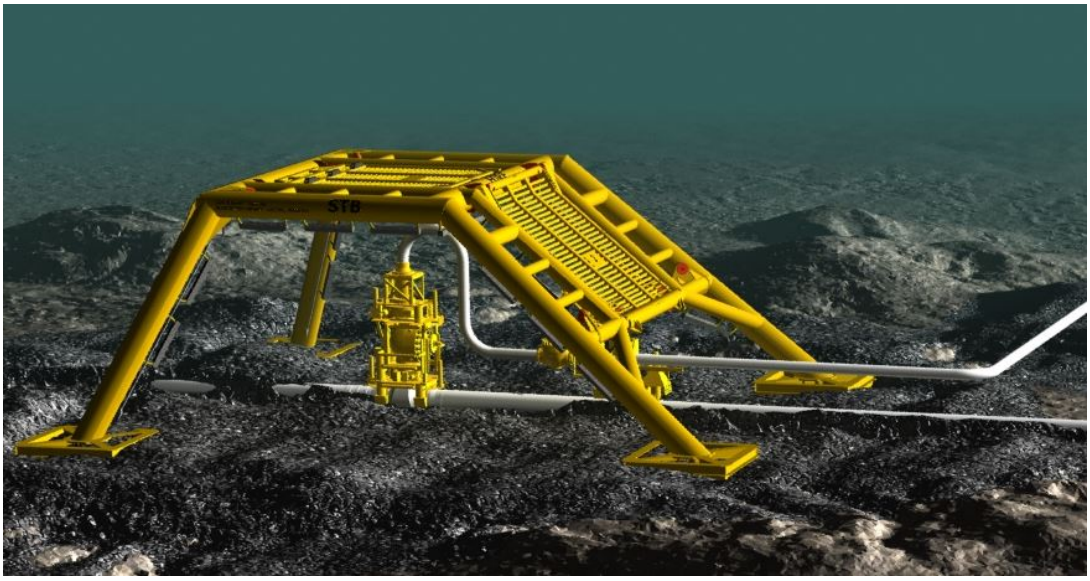

Figure 17: Simulation of the PS HHT protecting an oil installation [2].

4.1.3 Why the HTT PS?

The reasons for choosing the HTT PS as a study case are quite simple. As mentioned earlier the HHT PS is rather small compared to other sub-sea structures employed in offshore engineering. However, its simplicity and the fact that its small dimensions indicates that all of the four legs will move in phase with each other, makes the computations easier rather than with more larger, complex systems.

Of course, having environmental risk in mind, there is a much greater hazard associated with the failing of constructions like platforms or pipelines rather than with small-sized protections structures. The fact, however, is that there exists an extensive amount of research where just these structures are considered, while little is written on smaller constructions. In addition the personal interest of the author lies within learning the general theory concerning earthquake loadings on sub-sea structures rather than focusing explicitly on a complicated structure which would be more time consuming.

4.2 Finite Element Modelling and Analysis

Based on the construction drawings provided by Reinertsen AS [2] three different finite element (FE) models of the study case were constructed in Abaqus/CAE:

1. A fixed base model.
2. A model with springs and dashpots between the structure base and the ground to simulate the effects of SSI.
3. A model with springs and dashpots, and in addition buoyancy, drag and inertia loading, and added mass to simulate the fully submerged structure.

The structure itself was modelled as a three-dimensional frame with only its main members, hatches and pads included. In the early stages of the modelling process the idea was that only the main members and pads were to be included. But as the hatches provide a significant "dry" mass of 5.0 and 5.1 tons and also contribute to the stiffness of the structure, they were included later on.

Only wire-features were utilized as shown in figure 18, and minor details, as stiffeners for instance, were ignored as these contribute little to the overall stiffness and mass of the structure.

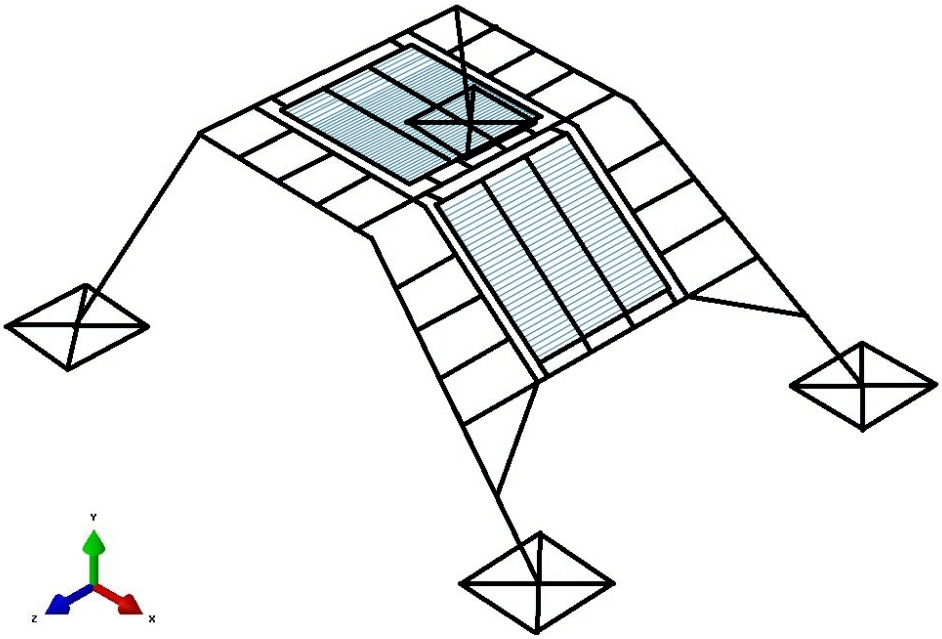

Figure 18: Modelling of the HTT PS using wire features.

The dimensions of the main members are consistent with the data provided in the construction drawings, whereas the geometry and dimensions of the remainder of the model are somewhat adjusted by the author;

- In modelling the pads only the HE300B beams were included as they provide most of the stiffness and mass in the elements that make up the pads.

- The connection between the frame and the hatches were modelled by very stiff wire features to ease the modelling, whereas these connections in reality are much more complex.
- Due to lack of detailed information on the members in the hatches, the geometry and dimensions of the hatches were constructed based on the overall hatch geometry and the total weight of each hatch.

The finite element employed is the Timoshenko beam element as this allows for transverse shear deformation [18]. In order to determine a proper size of the elements, a crude convergence analysis was performed in Abaqus shown in figure 19.

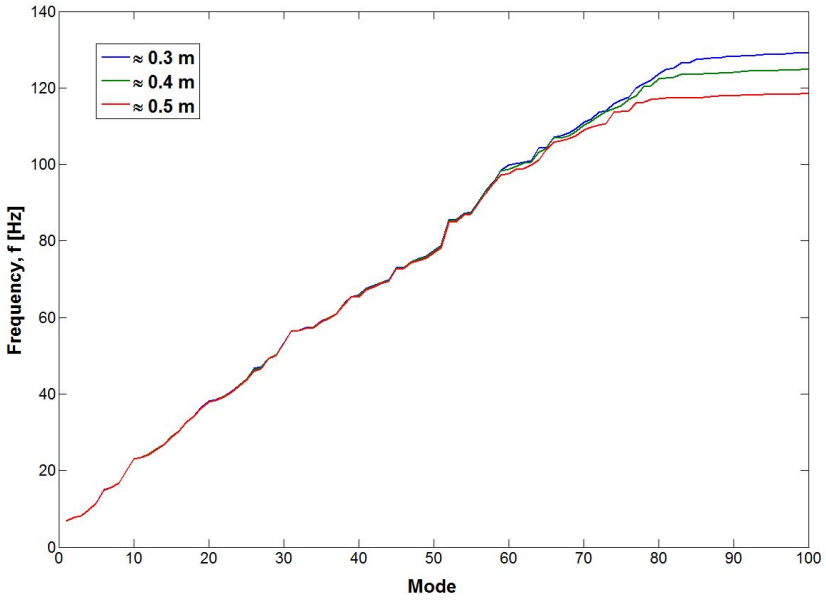

Figure 19: Convergence check by eigenfrequencies.

As there is so to speak no difference between the frequencies for most part of the modes, a mesh of approximately 0.4 m is used. A smaller mesh size was originally used for the pads, but the computational cost proved to be much larger than the reward in convergence. Although it would be more correct to use a frequency dependent damping model, structural damping was introduced through Rayleigh damping. The first mode of the system is assigned a damping of 1 % of the critical damping ratio. Using this model means that the structural damping remains "constant" for all three models, and thus the results will only differ by means of the springs and dashpots introduced in the SSI model and the fluid forces introduced in the FSI model.

In the following subsections a more detailed description of the three modelling cases are presented, with focus on both the modelling itself and discussion upon the choices that have been made along the process.

4.2.1 Model with fixed base

To shed light upon the importance of SSI a model with fixed base was created for comparison reasons. As mentioned earlier the pads have short skirts that penetrate the seabed, and with the possibility of overlying rock the degrees of freedom (dof) at the connection between pads and frame are to a degree constrained. Therefore the pads were modelled as fixed with respect to all dofs as shown in figure 20 where the profiles of the different members are made visible.

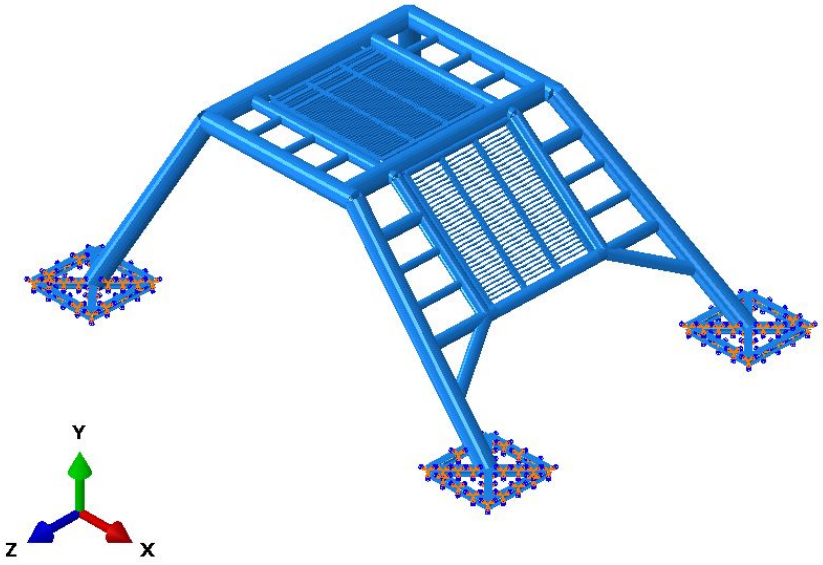

Figure 20: Model with fixed base.

4.2.2 Model with SSI effects included

In chapter 2.1.2 various models for simulating SSI were presented. In this case the procedure with springs and dashpots between structure and ground were used. Each base is connected to springs and dashpots in 61 evenly distributed nodes, where the springs and dashpots act in all six degrees of freedom as shown in figure 21.

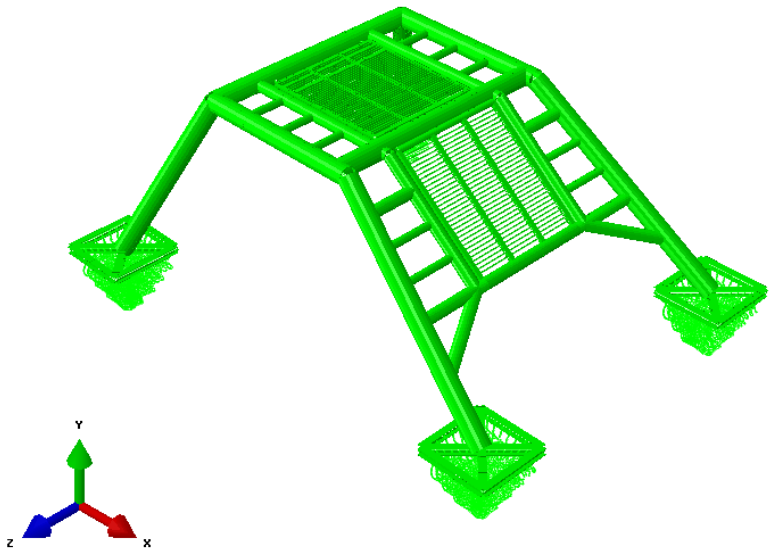

Figure 21: Model with springs and dashpots between the base and the "ground" nodes.

Several attempts were made in Abaqus to model these spring/dashpot combinations. As the author have understood from the documentation provided with the software there is a possibility of using connector elements in the assembly module that have the same function as the springs and dashpots that can be generated in the part module. However, both methods require that the connection has to be between nodes, and therefore a reference point was used for each leg. The spring/dashpot combinations in the part module were employed. As the legs of the HTT PS are expected to move in phase, the accelerations were applied at the reference points.

Further, the question of stiffness and resistance in the spring/dashpot combinations has to be addressed. As presented in section 2.1.2, for the method chosen, these properties depend on the shear wave velocity, the density, and Poisson's ratio of the soil. According to Yokota and Konno [39] a Poisson's ratio of 0.5 is representable when the clay is saturated and perfectly undrained. Hamilton [23] presents data from marine sediments in the Indian Ocean, the Japan and Bering Seas, the Atlantic Ocean, Caribbean Sea and Gulf of Mexico where the Poisson's ratio varies from about 0.497 at the sea floor to 0.412 at a depth of 1000 m for in situ, water saturated silt clays, turbidities and mudstones. Based on these data and due to the lack of data concerning the soil at the Halten Terrace, a Poisson's ratio of 0.96 is used in the computations.

The density of the soil is assumed to lie somewhere between 17 and 21 kN/m^3 which is typical densities for Norwegian sediments [20]. A plot of the first natural period for

various shear wave velocities is shown in figure 22 for the two limit values of the density. The red line represents the first natural period of the fixed model. As can be seen from the figure, the natural period of the SSI-model approaches the fixed period as the shear wave velocity increases - the stiffness and damping in the soil represented by springs and dashpots increases with increasing shear wave velocity and approaches a "fixed" state. Also, there is little difference between the periods obtained with the two densities. Therefore a density of 21 kN/m^3 is utilized for this study case as this density provides periods that are closer to the fixed period when the shear wave velocity increases.

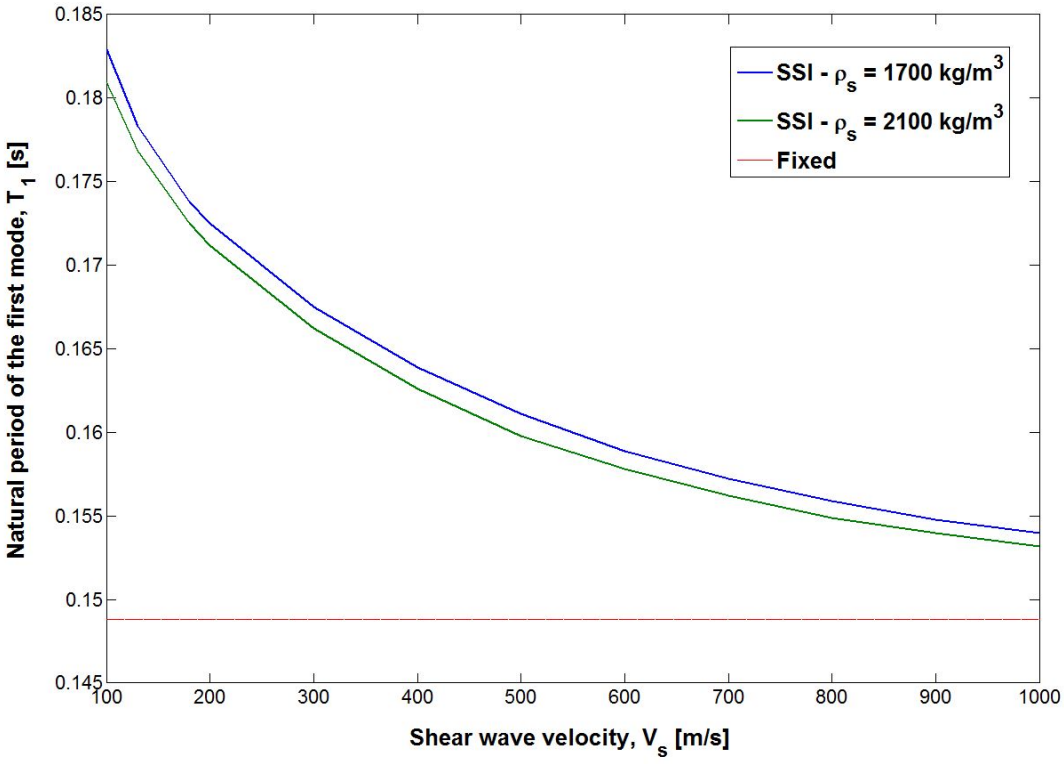

Figure 22: Model with springs and dashpots between the base and the "ground" nodes.

As for the shear wave velocity, Eurocode 8 divides the soil into different types as shown in table 2. The soil at the site is assumed to consist of soft clay but presumably it is firm enough to be able to support the structure at hand. This would suggest a ground type somewhere in between type D and S_1 as the author sees it. Ground type S_1 with a large plasticity index and high water content seems rather drastic as this would indicate a near liquid-like state when the water content is high. If using the maximum shear wave defined for ground type D, the behaviour may be more like that of more coarse-grained soil types with pebble granules, sand, silt and clay for example. As a compromise between the two types and due to lack of knowledge on details of the soil type, a shear wave velocity of 150 m/s is used in the computations.

4.2.3 Model with SSI/FSI effects included

To get an idea on how the HTT PS behaves in its real environment the SSI model presented in the previous section was modified to include the loads that are expected to arise when it is installed. With currents and waves, and the possibility of earthquakes, forces related to drag and inertia as presented in section 2.1.3 will occur, and there will be a hydrostatic pressure, buoyancy forces, and a temperature difference between the surface and the seabed as well.

For the sake of this study, it is more interesting to get a "clean" look at the dynamic side of this environment rather than the static. Of course, there will be some prestress in the structure due to cooling of the material as the structure is lowered towards the seabed and due to hydrostatic pressure, but this prestress is assumed to have little influence on the dynamic behaviour compared to the forces that will arise when the structure is subjected to ground accelerations. Therefore, the presence of hydrostatic pressure and a temperature difference are ignored. For the same reason the water is assumed to be still, with no currents or waves present.

To simulate this fluid-structure interaction, Morison's equation, with reference to section 2.1.3, is used. This may be a rather crude approximation to reality since this equation is derived on the basis of a single cylinder subjected to free-stream fluid flow perpendicular to its longitudinal axis. In, reality, when earthquakes do occur, the motion of a structure located at the bottom of the sea will be characterized by rapid movements back and forth in all six degrees of freedom. This will cause separation and a turbulent flow around the members of the structure almost instantly, meaning that there is no steady laminar flow and predictable pathways of the fluid particles by the opinion of the author. This is specifically the case for the hatches, where there is a small distance between the components. However, the equation is assumed to sufficiently predict fluid forces for this case study as the goal is to see the differences between "dry" and "wet" environments rather than getting an "exact" answer with regards to flow patterns for instance.

Using Morison's equation means some knowledge on both fluid and structural components be needed. As assumed above, the motion of the structure during an earthquake is likely to cause fully developed separation and a turbulent flow pattern, and a high Keulegan-Carpenter (KC) number is therefore expected. Further, since the flow is assumed to be turbulent, we are dealing with a Reynolds number larger than at least $Re_{cr} > 10^5$ according to Crowe [17]. This is known as the critical point where the flow is no longer laminar, and since it is assumed that the flow is fully turbulent a Reynolds number greater than the transition point, $Re_{tr} = 3 \cdot 10^6$, is assumed. This type of flow is by Faltinsen [21] characterized as transcritical flow, and it is suggested that typical drag and mass coefficients for a smooth circular cylinder at $KC > \approx 40$ are:

- $C_D = 0.7$
- $C_M = 1.8$

The drag coefficient given above is as the author sees it a coefficient for the normal drag force. As the motion of the structure is rapid and restricted to small amplitudes of displacement it is reasonable in the author's eyes to regard the normal drag force as

the dominating one compared to tangential drag force, and therefore the tangential drag coefficient is assumed to be zero. This assumption is of course not consistent with how the drag forces behave in reality, but for the purpose of this thesis it is assumed to be a valid assumption.

In addition to the forces given by Morison's equation we also get an additional "added mass" or virtual mass as given in equation 2.1.21. This mass is computed based on the added mass coefficient, which by the mass coefficient given above leads to:

- $C_A = 0.8$

Implementation of these forces in Abaqus was mostly done by editing the "keywords" related to the input file. Also buoyancy forces were accounted for here, while the added mass was implemented by defining it as a sectional property. In addition, the Abaqus documentation is somewhat unclear on the subject of full immersion of an element. All the main members of the PS HTT are filled with water, thus providing some extra inertia forces during dynamic events. The author sees it as the elements are fully immersed, but they are not filled with water inside when specifying the added inertia as has been done. Therefore, the density of the main members are increased according to the amount of water within the members, and the density of the water.

4.2.4 Studies performed

The purpose of this thesis is as presented earlier to get an idea on how a given structure behaves under certain conditions when subjected to base accelerations. To investigate this, the three models presented in the foregoing sections were created in Abaqus. The studies performed on these models are summarized as follows:

1. The undamped eigenfrequencies and eigenmodes of the models were extracted and compared to investigate vibration properties of the models.
2. The participation factors of the three models were compared in order to identify the modes that contribute most to the response, and thus determine how many modes to employ in the modal analysis.
3. A geometrical nonlinear dynamic analysis was performed on all three models by means of direct, implicit integration. The acceleration histories used are those obtained for the Åsgård field.
4. A linear modal modal dynamics analysis was performed on the FSI model. The acceleration histories used are those obtained for the Åsgård field.
5. An evaluation of the structural performance was performed by running a nonlinear dynamic analysis by means of direct, implicit integration for the FSI model with acceleration histories obtained for the Statfjord field.

The results are presented in the following section along with an evaluation of these results.

5 Results and discussion

In this section the results obtained in this thesis is presented and discussed. Firstly a short discussion regarding the process of finding a representative ground motion response parameter for a given return period is discussed. The subsequent sections presents results for the analyses performed on the HTT PS and an evaluation of the structural performance.

5.1 Discussion regarding results found by probabilistic earthquake simulation

The earthquake catalogue generated in this context has an element of uncertainty to it as the coefficients extracted from the zonation report [4] is used without the appurtenant weights as it is not known how to employ these weights. Figure 23 shows the distribution of magnitudes for the number of earthquakes generated found by one of the simulations. When drawing a line through the top mid point of the bars a curved line is displayed. Ideally this should be straight as the Gutenberg-Richter relationship is a linear relation.

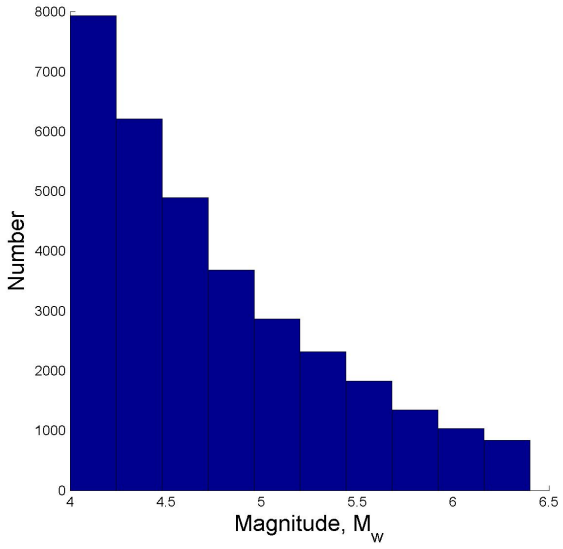

Figure 23: A plot of magnitudes versus number of earthquakes found in the generation of a synthetic earthquake catalogue.

It is suspected that this "flaw" is projected to the resulting Gumbel distribution of the ground motion parameter in question. When running the script provided in the electronic attachment, the PGA for a given period varies too much between simulations to be reliable. As the attenuation relationship employed and the model used for performing order statistics are assumed to be correct it is highly possible that this variation in PGA_R results from variations in the synthetic earthquake catalogue generated. Due to this uncertainty, the procedure in section 3 was performed 49 times and the resulting median earthquake corresponding to the return period chosen was extracted.

5.2 Vibration properties of the HTT PS

The vibration properties of a structure plays a significant role in the response of the structure when subjected to dynamic loading. To see how these properties develop with the introduction of SSI and FSI an undamped frequency analysis was performed on each of the three models.

Table 6 lists the first ten eigenfrequencies of the three models. First of all, the eigenfrequencies are quite high for all three models, which in turn indicates that the structure inhibits a stiff behaviour when subjected to dynamic loading. Secondly, it is noticed that for each mode, the eigenfrequencies decrease with the introduction of springs and dashpots at the base, and fluid forces for the FSI model. This is in terms with the theory presented in section 2.1. In other words, the behaviour of the submerged structure is much more flexible than the onshore structure with a longer natural vibration period.

Table 6: Eigenfrequencies for the three models.

Mode	Frequency, f [Hz]		
	Fixed model	SSI model	FSI model
1	6.7197	5.7202	4.4722
2	7.8122	6.2571	4.5296
3	8.0427	7.7434	6.3936
4	9.6968	8.8826	7.6883
5	11.4090	9.0198	8.0919
6	14.8880	13.5570	10.3060
7	15.5550	14.7450	11.7440
8	16.6150	14.8620	12.9390
9	19.9150	17.2580	14.2960
10	23.0520	18.4190	14.7450

Furthermore, an interesting change in the mode shapes of the structure is depicted in figure 24. For the first mode, the shape is similar for the three models, but for the second mode the shape changes when going from fixed base to springs and dashpots in the SSI model. This shape is in turn represented for the third mode of the fixed model. Even more interesting is the diagonal transformation represented by figures 24d, 24h and 24l. Although there is no clear pattern with regards to how and when the mode shapes change, it is clear that when introducing new stiffness and inertia forces to the structure its vibration properties change. The ten first mode shapes are displayed in the appendix in section B.

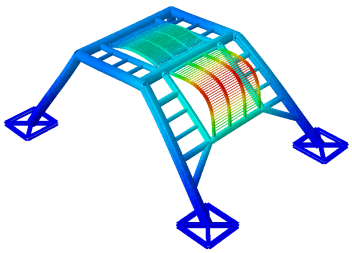

(a) Fixed, 1st mode

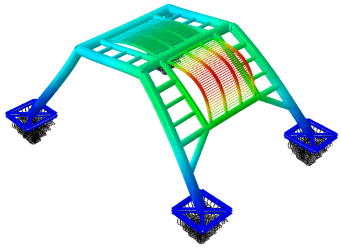

(b) SSI, 1st mode

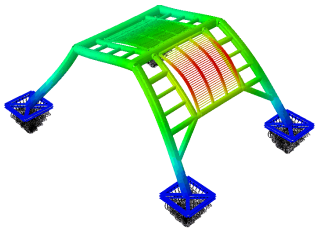

(c) FSI, 1st mode

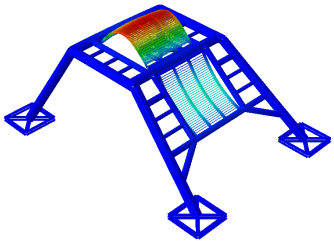

(d) Fixed, 2nd mode

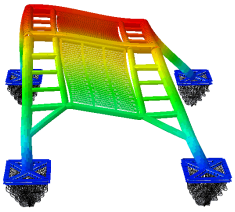

(e) SSI, 2nd mode

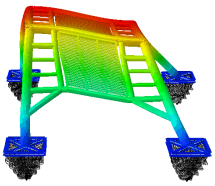

(f) FSI, 2nd mode

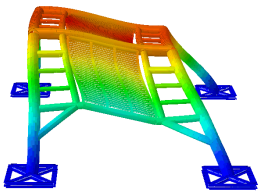

(g) Fixed, 3rd mode

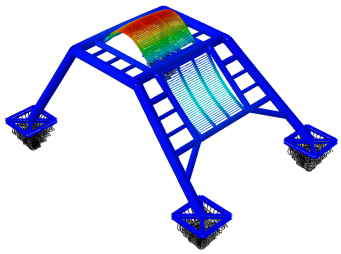

(h) SSI, 3rd mode

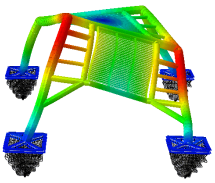

(i) FSI, 3rd mode

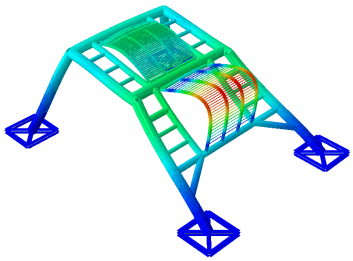

(j) Fixed, 4th mode

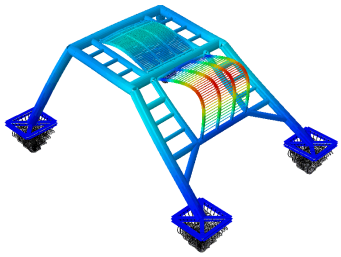

(k) SSI, 4th mode

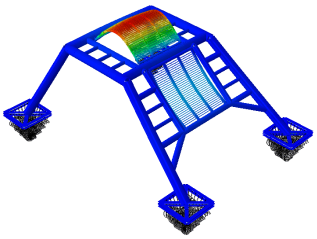

(l) FSI, 4th mode

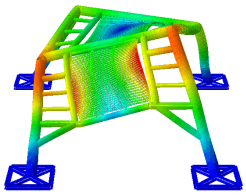

(m) Fixed, 5th mode

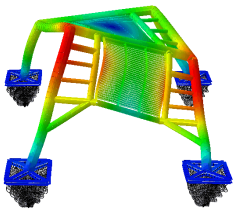

(n) SSI, 5th mode

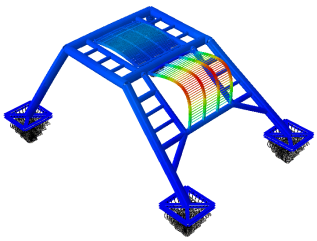

(o) FSI, 5th mode

Figure 24: Eigenmodes for the three models - number 1-5.

5.3 Response properties

Referring to section 2.2.1 it is evident that by inspecting the participation factors related to each of the modes of a structure, one can make some assumptions regarding which modes that will contribute to the structural response. The participation factors in all six dofs are computed automatically by Abaqus [18] during a frequency step, however, for simplicity only the translational participation factors will be discussed in this context.

Figure 25 shows the participation factors in the x-direction for the 100 first modes. The two other translational participation factors are given in the appendix in section C. The blue bars in the figure represent the positive participation factors, whereas the red bars represent the absolute value of the negative participation factors.

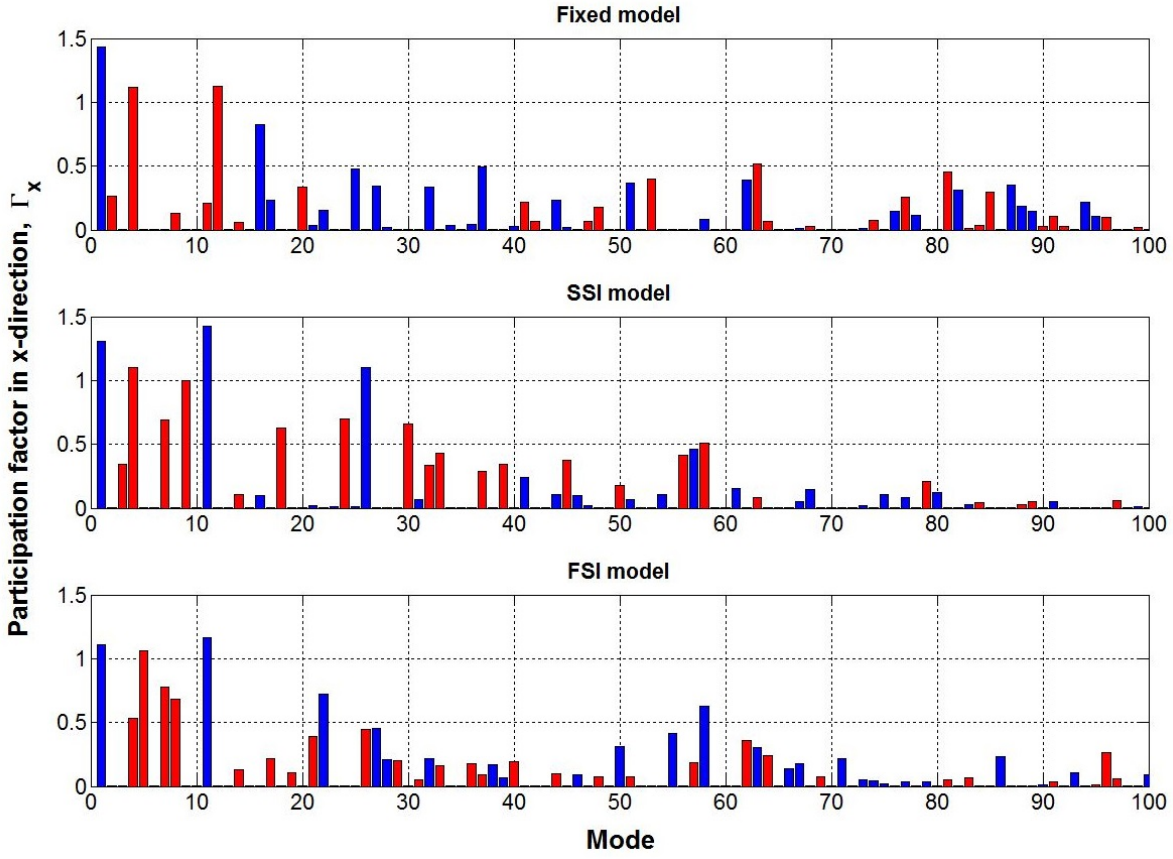

Figure 25: Participation factors of the first 100 modes in the x-direction for the three models.

By looking closer at the signs of the participation factors and remembering equation 2.2.12 it is clear that there is a correspondence between the modes depicted in figure 24 and the participation factors. Figure 26 displays the signs of the participation factors for the five first modes of all three models. The x-direction is in the direction of the longest side of the structure, the y-direction is vertical and the z-direction is in the direction of the shortest side of the structure as shown in figure 18.

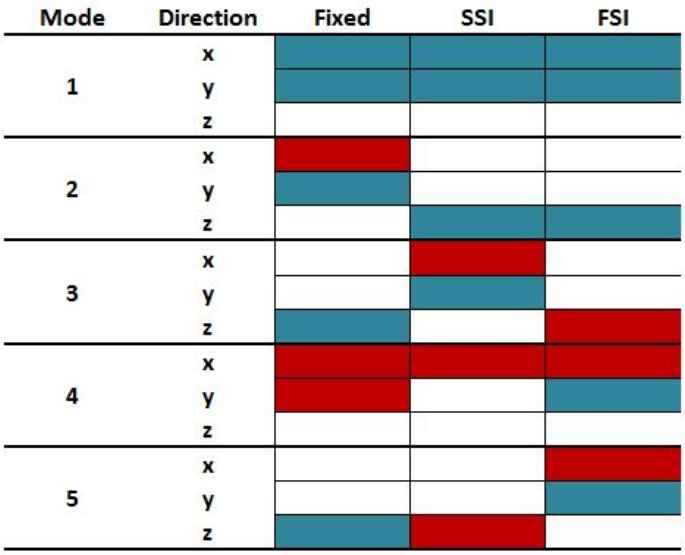

Figure 26: Figure depicting the signs of the participation factors. Blue: positive; red: negative; blank: zero.

The first mode have the same shape for all three models referring to figure 24, but as it can be seen, the shape becomes more "magnified" with the SSI and the FSI models. Compared to figure 25 this can be connected to the decrease in $\Gamma_{x,1}$ from the first model to the last. For the second mode shape the participation factors in the x- and y-direction have non-zero values for the fixed model, whereas these values are zero for the SSI and FSI models. The only non-zero values here are those in the z-direction. Thus rendering the second mode shape for the SSI and FSI models. Lastly, considering mode shape number five for the fixed model and the SSI model, and the signs of Γ_z for this mode shape, it is evident that there is full correspondence between the signs of the participation factors and the appurtenant mode shapes.

Now that equation 2.2.12 has been "visually" discussed through the foregoing paragraphs, it is of greater importance to discuss the magnitude of the participation factors. By equation 2.2.15 it is clear that the modes that contribute the most to the response are the ones possessing the largest absolute values. Consulting figure 25 it is seen that for the x-direction, the ten first modes play a significant part in the response for all three models. For the next ten modes, it is clear that there is a shift in the response as the nonzero modes of the fixed model are approximately zero for the SSI and FSI models.

Figures 37 and 38 in appendix C display a similar trend in the magnitude of the participation factors for the y- and z-direction. For the response in the x-direction, modes 1-30 seem to contribute the most, whereas for the y- an z-direction it seems reasonable that the first 20 modes will produce a viable solution referring to the response in the appurtenant directions.

In order to find out how many modes that will suffice for providing a reasonable response history, one can run a frequency analysis in Abaqus, rendering the fraction of total mass accounted for by the number of eigenfrequencies chosen, and the total generalized mass they account for, as is done in an example in the Abaqus documentation [18]. This

was only done for the FSI model, and the results showed that using 20 modes covers approximately 88 % of the total mass, while using 30 modes covers about 91 % of the total mass in all three translational directions. Thus the 20 first modes were used in the modal analysis as the difference between the two alternatives presented here is trifling.

5.4 Numerical response analysis

The numerical response analysis was carried out in Abaqus using the HHT α-method presented in section 2.2.2 with an algorithmic damping of -0.05 as is the default in Abaqus [18]. Geometric nonlinearity was accounted for in the analysis, and the resulting relative displacement histories for the node marked with the red dot in figure 27 are presented in appendix D.

For convenience, only the relative displacement for the three models in the x-direction will be discussed here as this holds for all three directions due to similar characteristics. The horizontal relative displacement in the x-direction is shown in figure 28. Overall, the displacements are quite modest. Since the SSI model is less stiff than the fixed model it produces a larger amplitude than the fixed model as mentioned in section 2.1.2, but as the mass of the two models is the same they oscillate about the same axis. The FSI model on the other hand, which is more massive and is subjected to fluid forces, oscillates about an axis even farther away from the initial state.

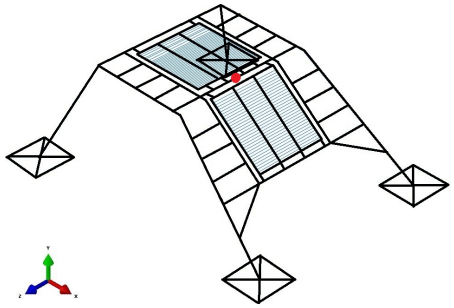

Figure 27: The node used for comparing displacement histories.

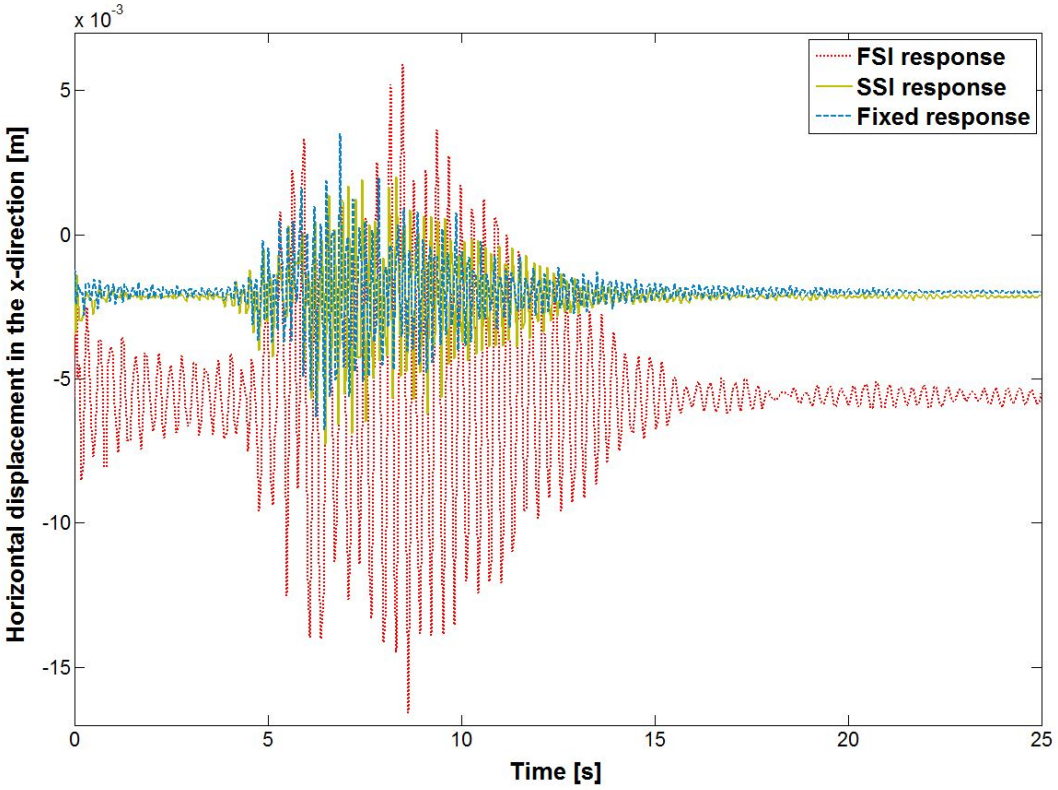

Figure 28: Horizontal displacement history in the x-direction.

This moving of the axis of oscillation is as the author sees it due to the introduction of geometric nonlinearity. The top hatch of the model weighs about 5 tons meaning it will transfer fluctuating forces and moments to the beam at which the node in question is located. Initially, the way the analysis has been carried out in Abaqus, the structure is subjected to a gravity load, which means the weight of the hatch and the construction itself will remove the node in question away from its initial state in the negative x-direction due to the overall geometry of the structure. Thus, when the ground accelerations are imposed at the base, the response will be computed from the deformed geometry rendering a shift in the axis of oscillation depending on the weight of the structural elements.

The FSI model is constructed in the way that the density of the elements are larger than that of the fixed and SSI models, and in addition there are fluid forces acting on each of the structural elements. This increase in density is to account for the water inside the structural components. With this new density, the model weighs almost twice its originial weight. This results in twice as large inertia forces, larger amplitude and an extension of the period of the oscillation.

Also, the amplitude of vibration at the start of the analysis is relatively large for all three models at the instant the base acceleration is imposed. Then it decrases for a few seconds before the ”real” base acceleration is imposed. This is simply due to inertia forces. When the structure is suddenly put into motion, even though the acceleration is small, it will take some time before the structure adjusts to the base acceleration and reaches a steady state of vibration. As can be seen the displacements are quite small indicating that drag forces in practise will be quite modest and that the inertia forces dominates the structural motion.

When it comes to the structural performance during this seismic event, this will be discussed in section 5.6 as it is more convenient for reasons related to the modelling procedure.

5.5 Modal response analysis

In reality, one might say that all structures inhibits some source of nonlinearity, but in many cases a linear analysis of a problem will produce a good enough estimate on structural response to external loading. To investigate if this was true for the HTT PS, a modal analysis was performed based on the 20 first eigenfrequencies of the FSI model as presented in section 5.3 for the same node as was the basis for the numerically determined response. The modal damping was introduced through Rayleigh damping by assigning the first mode a damping ratio of 1 % of the critical damping. The resulting response histories in all three directions are provided in appendix E, while the response in the x-direction is also given in this section displayed in figure 29. For the sake of comparison, the results obtained for the displacements by numerical integration in the previous section are also plotted in this figure.

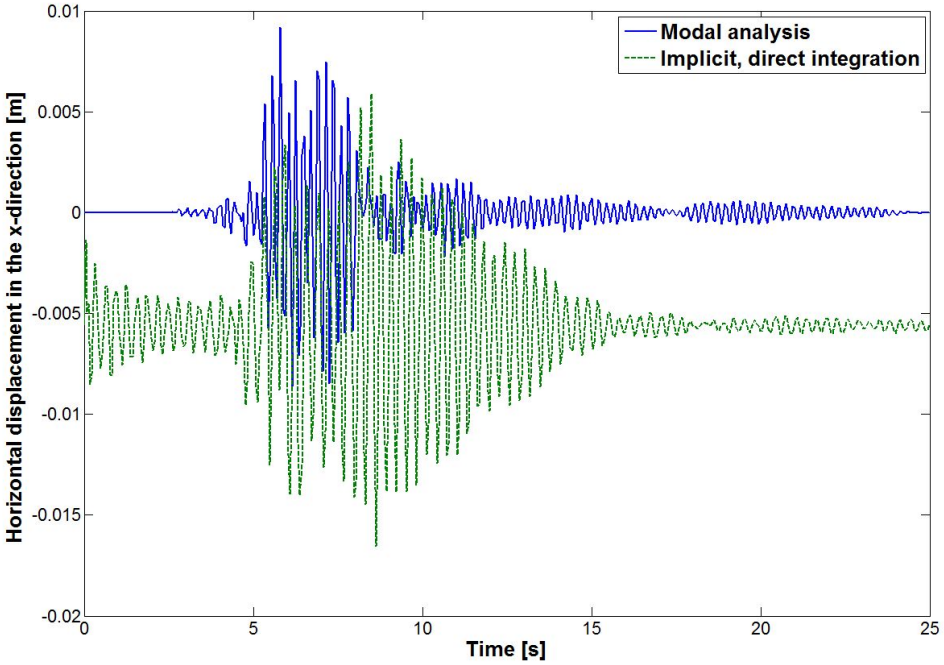

Figure 29: Horizontal displacement history in the x-direction generated by modal analysis for the FSI model.

By inspecting figure 29 it is clear that the computation of response is performed on the undeformed geometry. First of all, the axis of oscillation coincide with the initial state of the node which was not the case in the previous section. Secondly, since there is no initial deformation in the beam it will not respond to the small amplitude vibration it is subjected to until the acceleration escalates.

Comparing the displacement history obtained by modal analysis to the original acceleration time series for the x-direction given in figure 12 it is seen that the response is directly related to the acceleration time series. On the other hand, it is seen that the nonlinear approach renders much larger deformations of the beam which escalates rather than dissipates due to introduction of nonlinearity.

Considering the largest amplitude of vibration the modal analysis provides it is not so far off from that found by direct integration although the period of "large-amplitude" vibration is shorter for the modal results. Also, the modal analysis was performed within a time period of about five minutes, whereas the direct integration procedure took about four hours to complete. For response estimation the modal analysis is therefore an efficient way of coming to terms with what the "real" response might be.

In figure 30 below the maximum envelope von Mises stress for the modal analysis of the FSI model is presented (springs and dashpots are not shown). The maximum stress level of 312.9 MPa is located in the attachment elements located between the top hatch and the frame. This high level of stress is close to the yield limit of the material, and if considering safety coefficients used in design of steel structures it surpasses this design limit.

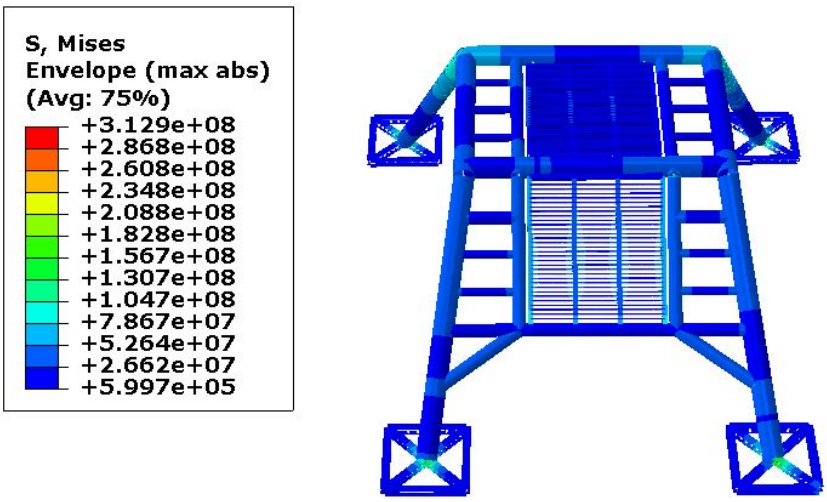

Figure 30: Maximum envelope von Mises stress in pascal occurring during the simulation of the Icelandic earthquake.

A discussion regarding the stress distribution for all the cases considered so far follows in the succeeding section.

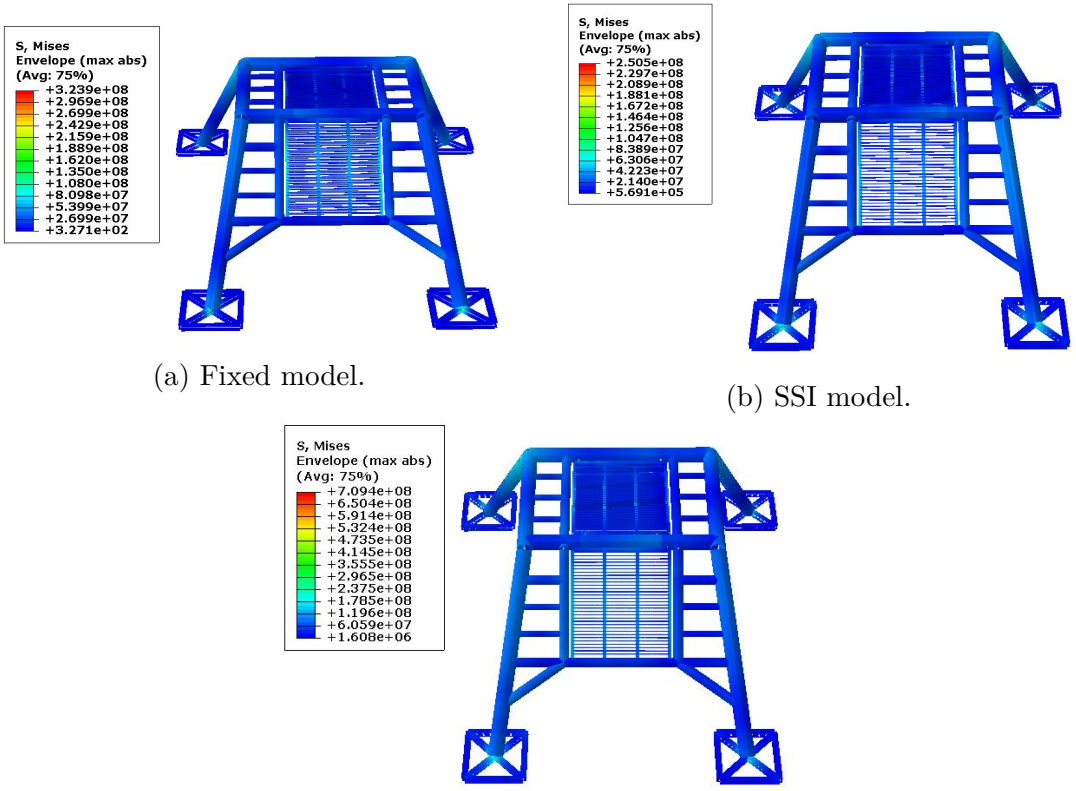

(a) Fixed model.

(b) SSI model.

(c) FSI model.

Figure 31: Maximum absolute envelope von Mises stress after the two first seconds of simulation.

5.6 Structural performance

When it comes to structural performance during the seismic events studied, the structure in general have no problems in withstanding the imposed base accelerations. For all the nonlinear displacement histories presented so far the initial amplitude of oscillation is considerably large as well as it changes rapidly with time. This indicates that large stresses will occur in the structure initially. However, these stresses are very concentrated - they only develop for the attachment elements between the hatches and the frame as for the modal response. The initial stresses have an order of magnitude equal to 10^{11} Pa. The components used to model this connection are simple cylinders of small radius and high stiffness. In reality they are more complex as can be seen from the construction drawings.This high stress level means that the response is no longer elastic, but rather plastic. The connections will thus undergo plastic deformation, but when failure of these connections occur is not known.

Above in figure 31 are the maximum envelope von Mises stresses that occurs after 2 seconds of analysis shown for all three nonlinear analyses performed so far. This is included to get an idea of how the structure responds when the base accelerations have their highest amplitude of vibration. As before, the maximum stress levels occur between the hatches and the frame.

As the author sees it, the hatch-frame connections will in real life be critical points as they have to transfer forces over a small cross-section. But as mentioned earlier they have a different geometry in real life which is more robust than the connection used in the modelling in this thesis.

To get another point of view on the structural performance the Friuli acceleration records were imposed on the FSI model. The displacement histories found by implicit integration are given in appendix F and in figure 32 for the x-direction, whereas the maximum envelope von Mises stress after the two first seconds of analysis are shown in figure 33.

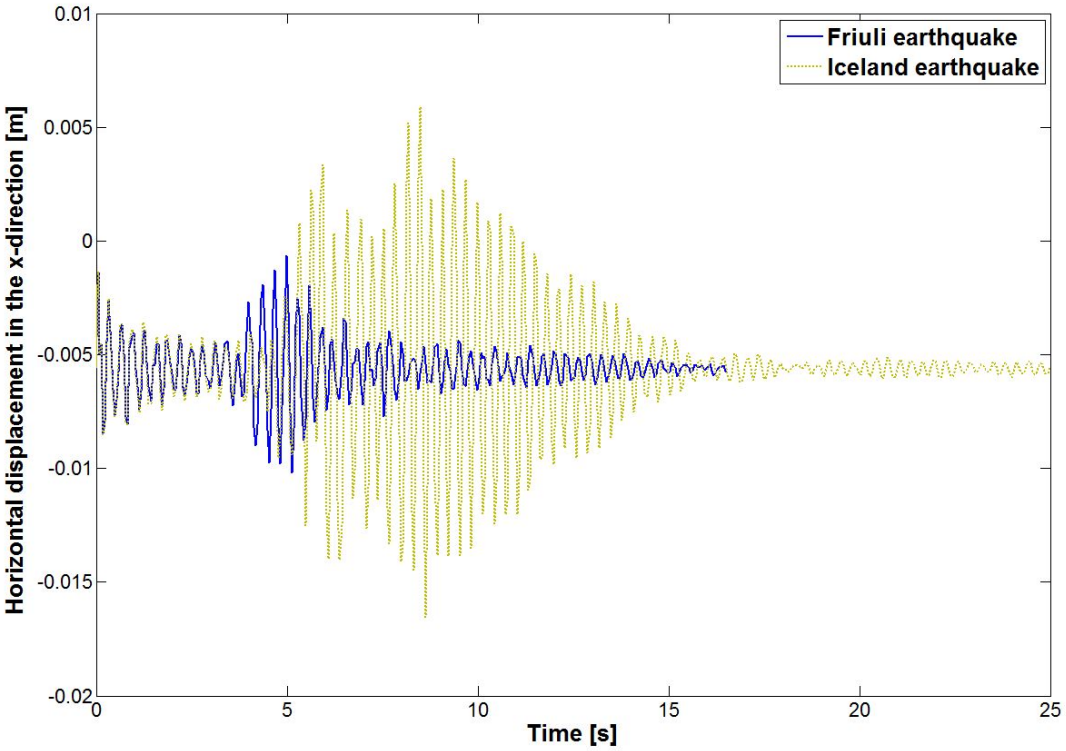

Figure 32: Horizontal displacement history in the x-direction for the Friuli earthquake.

Though the PGA of the Friuli earthquake is higher than that of the earthquake which occurred on Iceland it is seen from figure 32 that the displacements are of smaller magnitude. Comparing the respective acceleration time series in section 3.4 it is natural that the Friuli earthquake renders smaller displacements as the amplitude of acceleration is smaller than for the Icelandic earthquake. However the maximum envelope von Mises stress shown in figure 33 for this earthquake displays an even larger level of stress in the hatch-frame connections than presented by earlier analyses. As before, it is hard so say if this level of stress is representative for the actual response due to the modelling approximation by cylinders, but the same assumptions made for the stresses in figure 31 also holds here.

To conclude with reference to structural performance, the main frame will hold, but the connections between the hatches and the frame causes uncertainty as this is not modelled as given in the construction drawings. As the temperature at seabed may be somewhere between 4 and 10 degrees of Celsius, the material behaviour will be more brittle than if

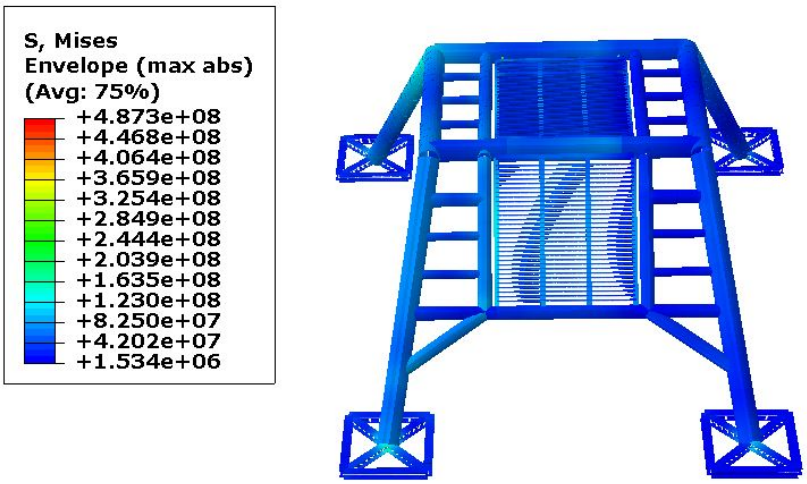

Figure 33: Maximum envelope von Mises stress after two seconds of simulation of the Friuli earthquake.

the structure was onshore rather than offshore (assuming it is summer). Thus if it in fact is so that the stress levels exceeds the yield limit in the connection elements, the period of which the material behaviour is plastic will be shorter than for the onshore structure and failure will occur at a smaller level of strain. Furthermore, although figures 31c, 30 and 33 may not tell the whole truth, they do point out the points on the structure which may be critical during a seismic event. Along with the connection elements between the hatches and frames, there is also a higher level of stress in the transition between the pads and the frame. As this is were the forces imposed by ground motion will be transferred to the construction, this is no surprise. As mentioned in section 2.1.2, with the introduction of SSI the overall demands on the structure tend to decrease. Comparing the subfigures 31a and 31b it is seen that the maximum stress is lower for the SSI model. Although this may be an inconclusive inference as there is some doubt regarding the discretization of the construction, it should be viable as the only change in model and analysis for the two cases is the introduction of springs and dashpots.

6 Conclusion and Recommendations

It is evident that the field of earthquake engineering comprises complex problems that often will have to be addressed by the use of statistical measures due to inconsistent, or too few data regarding previous earthquakes. The synthetic earthquake catalogue generated in this thesis is assumed to be too inconsistent, which in turn effects the probabilistic approach to finding a ground motion parameter for a given return period. However, by performing the procedure several times, the generated mean value of these runs will statistically provide a viable result in this context. All in all, the probabilistic approach employed in earthquake engineering is a powerful tool as one more than often find the amount of available data on earthquakes to be insufficient for the purpose of predicting possible future events.

To address the question of whether or not strong ground motions are a problem for the Norwegian offshore industry, the answer is no. So far, the industry operates in areas of low seismicity, which is expected for intra-plate regions. Thereby the offshore constructions are designed with this in mind. However, if oil production is to be started at Jan Mayen one might have to reconsider the hazard as volcanic ruptures followed by earthquakes are known to have happened. To put it in this way, possible earthquakes are not a problem as long as it is accounted for by the standards employed in the design of structures. At least this is assumed viable for operations on the Norwegian continental shelf as history has not produced a disastrous seismic event offshore, yet. As is known, the mid-Atlantic ridge is a location of higher seismicity than any of the currently producing fields and if oil is found near this ridge, the importance of seismic hazard assessment becomes even larger if one wishes to withdraw these deposits.

As for the study structure and the analyses performed on the three models of it, the results are as expected. Introducing springs and dashpots to the originally fixed model to simulate SSI renders larger displacements and lower stresses in the structural elements as implied in section 2.1.2. When introducing the fluid loads to the SSI model, the displacements of the structure are enhanced greatly. This is mostly due to the fact that with small displacements the inertia forces dominate the structural response. However, it is suspected that the method of increasing the density of the structural elements may induce some artificial weight on the structure components as the buoyancy force provided by the water within the structural elements is not accounted for. Thus, this renders a much heavier submerged construction than what can be expected in situ.

But what can be drawn from this is that the structure in questions is able to withstand the imposed ground accelerations. Of course, some of its components may gain some damage, but the overall structure is far from experiencing any remarkable signs of weakness.

Addressing the second research question of this thesis, it can be deduced from the analyses performed that for this particular structure the overall demands of the structure increases when fully submerged. This is mainly due to the inertia forces occurring below sea level. Additionally, the submerged structure experiences larger displacements than the ”dry” structure, though these displacements are very small.

However, this is a tiny structure compared to other subsea constructions. When the

structural dimensions becomes large, one has to consider that the supports may be out of phase, how massive the structural components are, how compact the structure is and so on. Furthermore, as the displacements found were so small, the drag forces hardly played a part. For long slender pipes for example the drag forces will probably have more to say as the displacements are of a totally different order than those discussed in this thesis. Thus, on the basis of what is found in this thesis, it is hard to say how other subsea structures will respond to seaquakes. However, we know that there will be fluid forces, and thus it is possible to address each problem individually, considering the geometry, material and spatial distribution of the structure.

As has been pointed out, there are some questions that have arisen along this process. These will not be further investigated in this thesis but will be mention here as a bases for further studies:

1. First of all, the problem of the varying PGA found by order statistics will have to be addressed to get a good estimate on what can be expected for each return period. This means figuring out what the weights provided in the zonation report [4] means as a first objective, and then evaluating the the results.
2. The water inside the structural components of the HTT PS may be modelled in a way that is not consistent with reality. Thus, if this is so, other options will have to be considered.
3. The zonation report used in this context is detailed with respect to Norway, but as new information has been published by SHARE [3] it is of interest to compare these maps and the underlying assumptions to see if there are any deviations.
4. As this thesis only considers one construction it is of interest to investigate other structures to see if some general assumptions can be made on the response of subsea structures involved in a seaquake.
5. Lastly, it would be interesting to not analyse one construction alone, but several structures, as they often make up a network of interconnected structures.

References

[1] Global earthquake model [web page]. [cited 10.06.13]. available from: http://www.globalquakemodel.org/.

[2] Private conversations with reinertsen as.

[3] Seismic hazard harmonization in europe [web page]. [cited 10.06.13]. available from: http://www.share-eu.org/.

[4] *Development of a seismic zonation for Norway: final report : prepared for Norwegian Council for Building Standardization (NBR).* NGI, Oslo, 1998. Omslagstittel: Seismic zonation for Norway.

[5] N. N. Ambraseys, J. Douglas, C. Berge-Thierry, P. Suhadolc, G. Costa, R. Sigbjörnsson, and P. M. Smit. Dissemination of european strong-motion data, vol. 2., 2004.

[6] N. N. Ambraseys, J. Douglas, S. K. Sarma, and P. M. Smit. Equations for the estimation of strong ground motions from shallow crustal earthquakes using data from europe and the middle east: Horizontal peak ground acceleration and spectral acceleration. *Bulletin of Earthquake Engineering*, 3(1):1–53, 2005. ISI Document Delivery No.: 091FF Times Cited: 150 Cited Reference Count: 61 Ambraseys, N. N. Douglas, J. Sarma, S. K. Smit, P. M. Springer Dordrecht.

[7] N. N. Ambraseys, J. Douglas, S. K. Sarma, and P. M. Smit. Equations for the estimation of strong ground motions from shallow crustal earthquakes using data from europe and the middle east: Vertical peak ground acceleration and spectral acceleration. *Bulletin of Earthquake Engineering*, 3(1):55–73, 2005. ISI Document Delivery No.: 091FF Times Cited: 15 Cited Reference Count: 19 Ambraseys, N. N. Douglas, J. Sarma, S. K. Smit, P. M. Springer Dordrecht.

[8] Jørgen Amdahl, Stig Berge, Anders Endal, Jørgen Hals, Håvard Holm, Tobias King, Carl Larsen, Leif Lundby, Torgeir Moan, Dag Myrhaug, Jonas Odland, Bjørnar Pettersen, Asgeir Søensen, Per Werenskiold, and Vilmar Æsøy. *Havromsteknologi: Et hav av muligheter.* NTNU, Samarbeidsforum Marin, Trondheim, 2011. Preliminary edition.

[9] H. Bungum, P. H. Swearingen, and G. Woo. Earthquake hazard assessment in the north sea. *Physics of the Earth and Planetary Interiors*, 44(3):201–210, 1986.

[10] Karl V. Bury. *Statistical models in applied science.* Wiley, New York, 1975.

[11] Karl V. Bury. *Statistical Distributions in Engineering.* Cambridge University Press, 1999.

[12] K. W. Campbell and Y. Bozorgnia. *Empirical Ground Motion Model for Shallow Crustal Earthquakes in Active Tectonic Environments Developed for the NGA Project.* Beijing, China, 2008.

[13] Enrique Castillo. *Extreme value theory in engineering.* Academic Press, Boston, 1988.

[14] W. F. Chen and Charles Scawthorn. *Earthquake engineering handbook*. CRC Press, Boca Raton, Fla., 2003.

[15] Anil K. Chopra. *Dynamics of structures: theory and applications to earthquake engineering*. Pearson Prentice Hall, Upper Saddle River, N.J., 2007. 3rd ed.

[16] Robert D. Cook. *Concepts and applications of finite element analysis*. Wiley, New York, 2002. 1. utg. 1974 4th ed.

[17] C. T. Crowe, D. F. Elger, B. C. Williams, and J. A. Roberson. *Engineering Fluid Mechanics*. John Wiley & Sons, 9th ed. edition, 2010.

[18] Dassault. *Abaqus software*. 2006.

[19] J. Douglas, F. Bungum, and P. Scherbaum. Ground-motion prediction equations for southern spain and southern norway obtained using the composite model perspective. *Journal of Earthquake Engineering*, 10(1):33–72, 2006. ISI Document Delivery No.: 025HG Times Cited: 16 Cited Reference Count: 85 Douglas, J Bungum, F Scherbaum, P Imperial college press London.

[20] A. Emdal. *Introduksjon til geoteknikk*. 2009.

[21] Odd M. Faltinsen. *Sea loads on ships and offshore structures*. Cambridge University Press, Cambridge, 1990.

[22] Google. Google maps, 2013.

[23] E. L. Hamilton. Vp-vs and poisson ratios in marine-sediments and rocks. *Journal of the Acoustical Society of America*, 66(4):1093–1101, 1979. ISI Document Delivery No.: HQ546 Times Cited: 101 Cited Reference Count: 0 Hamilton, el Amer inst physics Woodbury.

[24] Pall Imsland. The volcanic eruption on jan mayen, january 1985: Interaction between a volcanic island and a fracture zone. *Journal of Volcanology and Geothermal Research*, 28(1–2):45–53, 1986.

[25] Steven Lawrence Kramer. *Geotechnical earthquake engineering*. Prentice Hall, Upper Saddle River, N.J., 1996.

[26] K. M. Mathisen. Lecture notes from tkt4197 nonlinear finite element analysis. 2012.

[27] G. Moe. *Introduksjon til bølger og bølgekrefter*. Institutt for konstruksjonsteknikk, NTNU, Trondheim, 3 ed. edition, 2005.

[28] J. R. Morison, M. P. O'Brien, J. W. Johnson, and S. A. Schaaf. *The Force Exerted by Surface Waves on Piles*. 1950.

[29] N. M. Newmark and Emilio Rosenblueth. *Fundamentals of earthquake engineering*. Prentice-Hall, Englewood Cliffs, N.J., 1971.

[30] Standard Norge. Eurocode 8: Design of structures for earthquake resistance - part 1: General rules, seismic actions and rules for buildings, 2008.

[31] L. Ottemöller, H. H. Nielsen, K. Atakan, J. Braunmiller, and J. Havskov. The 7 may 2001 induced seismic event in the ekofisk oil field, north sea. *Journal of Geophysical Research: Solid Earth*, 110(B10):B10301, 2005.

[32] R. Sigbjörnsson and J. T. Snæbjörnsson. Probabilistic seismic hazard assessment toolbox. Technical Report 07002, 2007.

[33] R. Sigbjörnsson, J. T. Snæbjörnsson, and K. Bruun. *Probabilistic Seismic Hazard Assessment Toolbox - Modified*. 2013.

[34] S. Shyam Sunder and Ove T. Gudmestad. Earthquake time histories for the norwegian continental shelf. *Applied Ocean Research*, 10(2):100–105, 1988.

[35] Roberto Villaverde. *Fundamental concepts of earthquake engineering*. CRC Press, Boca Raton, Fla., 2009.

[36] E.L. Wilson, Computers, and Inc Structures. *Three Dimensional Static and Dynamic Analysis of Structures: A Physical Approach with Emphasis on Earthquake Engineering*. Computers and Structures, 2006.

[37] James F. Wilson. Dynamics of offshore structures (2nd edition), 2003.

[38] John P. Wolf and Andrew J. Deeks. Foundation vibration analysis - a strength of materials approach.

[39] K. Yokota and M. Konno. Dynamic poisson's ratio of soil.

Appendices

A Statistical Background - Extreme Value Statistics

A.1 Order Statistics

From an engineer's point of view it is more than often interesting to know the extreme values of a sample rather than investigate the whole sample. For instance, in connection with failure analysis one tests a number of specimen for what level of load they can tolerate before they fail. When these tests are completed, it is obviously more interesting to gather information about the lowest and/or the largest load levels rather than those in between. In other cases it might as well be the intermediate values that are significant, however, in this context we are more concerned with maxima and minima.

To perform order statistics on a sample, the sample has to be sorted according to size or magnitude. For some cases the sample is already in order, while in other cases the sample points must be rearranged. Adopting the notation of Bury [10], the sample points must be arranged such that

$$x_{(1)} \leq x_{(2)} \leq \cdots \leq x_{(r)} \leq \cdots x_{(n)} \tag{A.1.1}$$

where n is the number of sample points and x_i are realizations of the order statistic X. This means that $x_{(r)}$ is the realization of the rth order statistic $X_{(r)}$. This also implies that $X_{(r)}$ is a random variable until it is measured [10]. Further one can set a threshold value at which the values either lower or larger than that threshold are to evaluated. Stated another way, one chooses which tail of the ordered data one chooses to perform order statistics on.

A.2 Extreme value distributions

For the same reasons as stated in the previous section it is of interest to look at how the extreme values behave. There are three distributions that are commonly used to evaluate the distribution of extremes. As Bury [11] presents these in an elegant way, this section refers to his book entirely.

As the sample size increases, the distribution of the extreme value in question converges to one of the following three distributions:

- Type I model of maxima (Gumbel)
- Type II model of maxima (Frechet)
- Type III model of minima (Weibull)

In determining which distribution that is appropriate to use, one has to examine the distribution of the sample from which the extreme values were extracted from. If we

denote the distribution of the sample in the same manner as Bury [11] does, $f(y, \theta)$, it is the tail of $f(y, \theta)$ that must be evaluated.

If it is unbounded an decreases rapidly, the distribution of the extreme value is termed type I. For maximum extremes in samples from Normal, Log-Normal, Exponential, Gamma and Weibull distributions, this corresponds to utilizing the *Gumbel model* for the extremes with probability distribution function (pdf) given as

$$f(x; \mu, \sigma) = \frac{1}{\sigma} e^{-\dfrac{x-\mu}{\sigma}}; \qquad \sigma > 0; \quad -\infty < x; \quad \mu < \infty. \tag{A.2.1}$$

If the tail of the sample distribution has an unbounded upper tail, and in addition not all of its moments are finite, we are dealing with type II model of maxima. That means employing the Frechet model with pdf given as

$$f(x; \sigma, \lambda) = \frac{\lambda}{\sigma} \left(\frac{\sigma}{x}\right)^{\lambda+1} e^{-\left(\frac{\sigma}{x}\right)^{\lambda}}; \qquad x \geq 0; \quad \sigma, \lambda > 0. \tag{A.2.2}$$

This model is increasingly used for engineering purposes as it is very suitable for modelling phenomena where the largest maximum observations are unusually large.

If the tail is bounded however, the distribution model for the extreme is of type III. Dealing with minimum extremes in samples from the Log-Normal, Gamma, Beta, Frechet, and Weibull distributions, the Weibull model is the appropriate extreme value distribution to use. Its pdf for a continuous random variable X has the form

$$f(x; \sigma, \lambda) = \frac{\lambda}{\sigma} \left(\frac{x}{\sigma}\right)^{\lambda-1} e^{-\left(\frac{x}{\sigma}\right)^{\lambda}}; \qquad x \geq 0; \sigma, \lambda > 0. \tag{A.2.3}$$

In this context the distribution of the largest extreme values is of greater importance than the smallest extremes, hence the Weibull model is inappropriate to use but it plays a great role in other engineering problems.

B Eigenmodes of the three models

Through an eigenvalue extraction in Abaqus the undamped eigenvalues of the three models were obtained. The first ten eigenmodes are depicted in figures 34 and 35. The "figure-columns" represent the individual models, whereas the "figure-rows" represent the modes in ascending order.

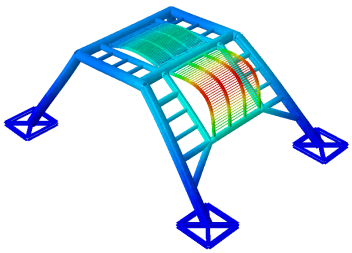

(a) Fixed, 1st mode

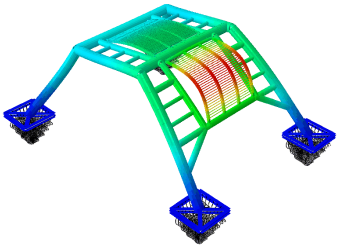

(b) SSI, 1st mode

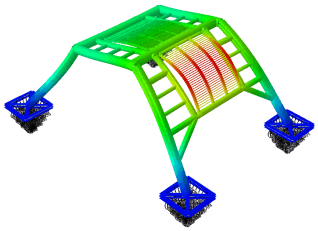

(c) FSI, 1st mode

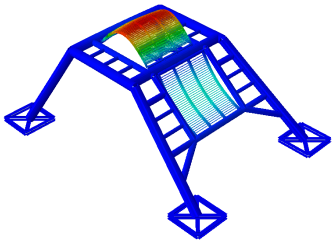

(d) Fixed, 2nd mode

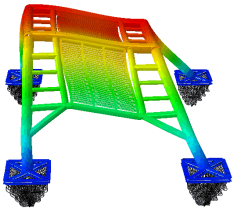

(e) SSI, 2nd mode

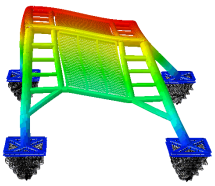

(f) FSI, 2nd mode

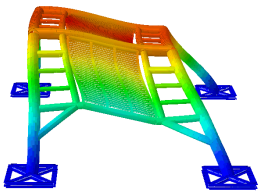

(g) Fixed, 3rd mode

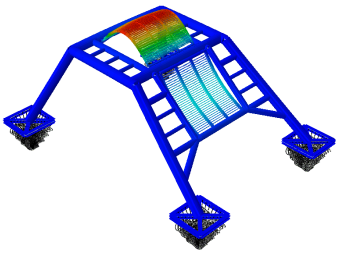

(h) SSI, 3rd mode

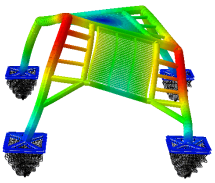

(i) FSI, 3rd mode

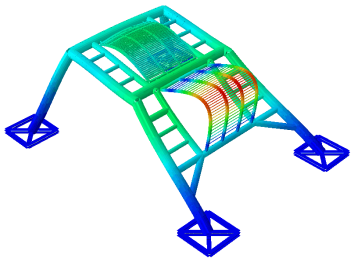

(j) Fixed, 4th mode

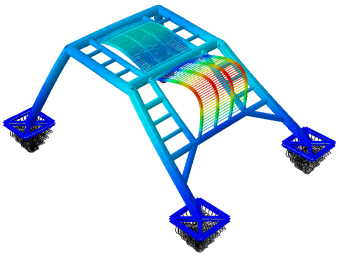

(k) SSI, 4th mode

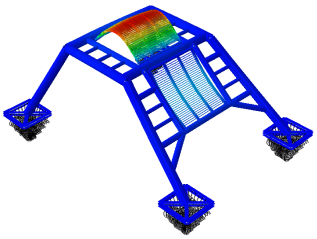

(l) FSI, 4th mode

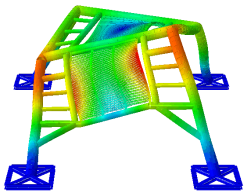

(m) Fixed, 5th mode

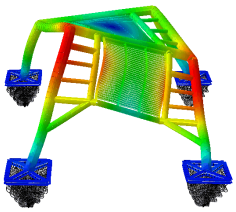

(n) SSI, 5th mode

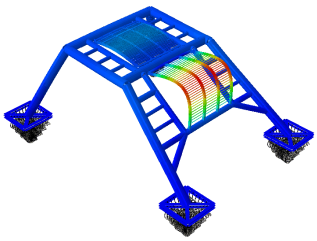

(o) FSI, 5th mode

Figure 34: Eigenmodes for the three models - number 1-5.

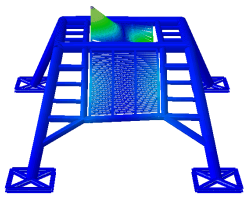

(a) Fixed, 6th mode

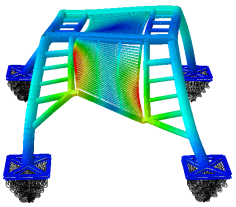

(b) SSI, 6th mode

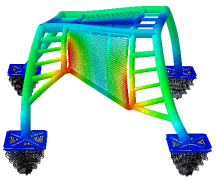

(c) FSI, 6th mode

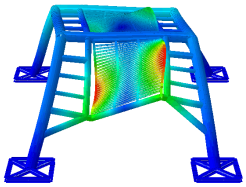

(d) Fixed, 7th mode

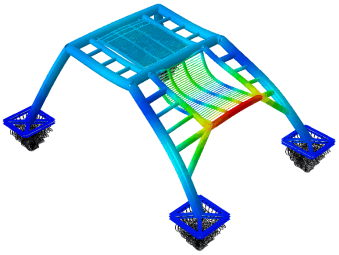

(e) SSI, 7th mode

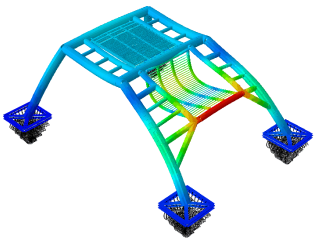

(f) FSI, 7th mode

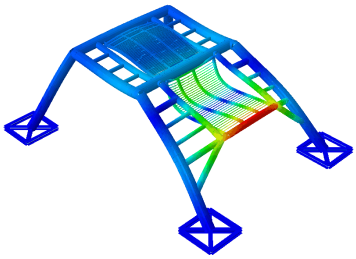

(g) Fixed, 8th mode

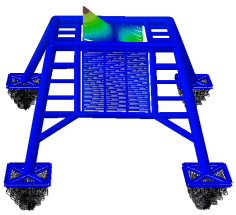

(h) SSI, 8th mode

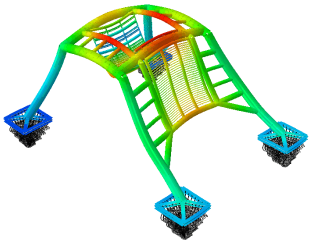

(i) FSI, 8th mode

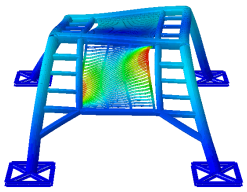

(j) Fixed, 9th mode

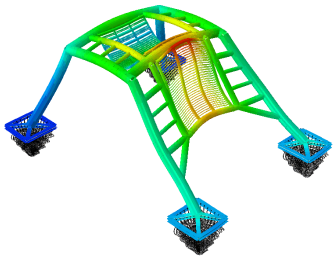

(k) SSI, 9th mode

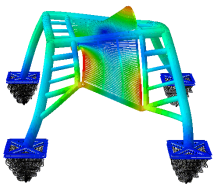

(l) FSI, 9th mode

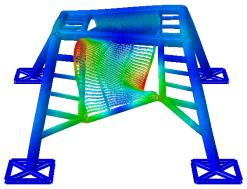

(m) Fixed, 10th mode

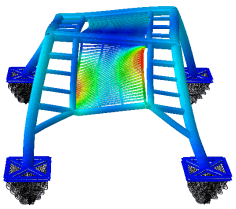

(n) SSI, 10th mode

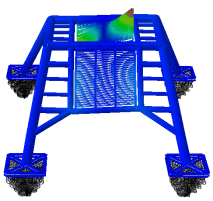

(o) FSI, 10th mode

Figure 35: Eigenmodes for the three models - number 6-10.

C Translational participation factors

The participation factors for the hundred first modes in the three translational directions are depicted in figures 36, 37 and 38. The blue bars represents positive participation factor, whereas the red bars represent the absolute value of the negative participation factors.

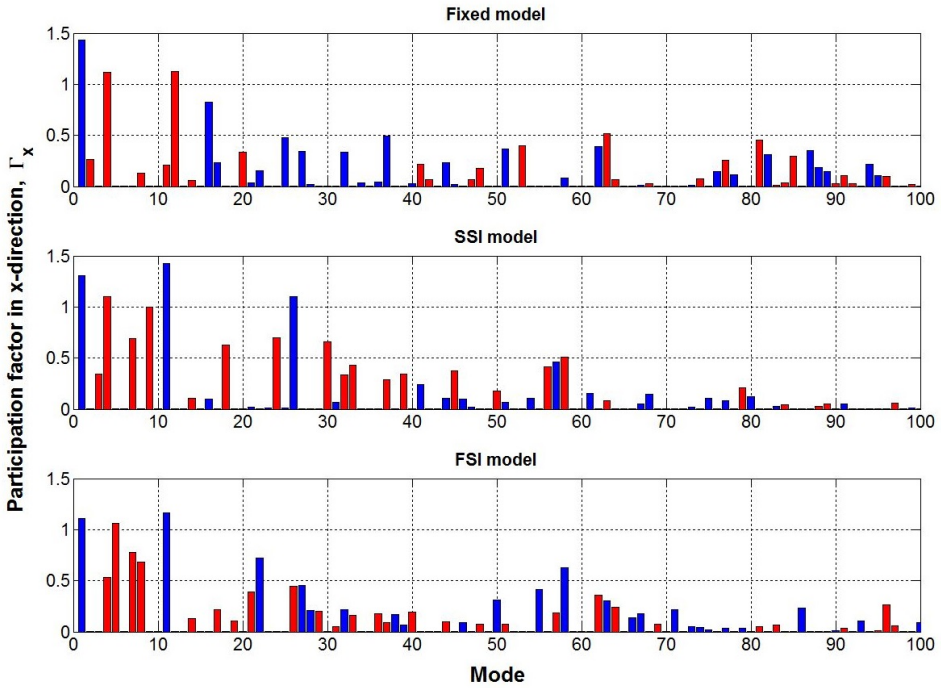

Figure 36: Participation factors of the first 100 modes in the x-direction for the three models.

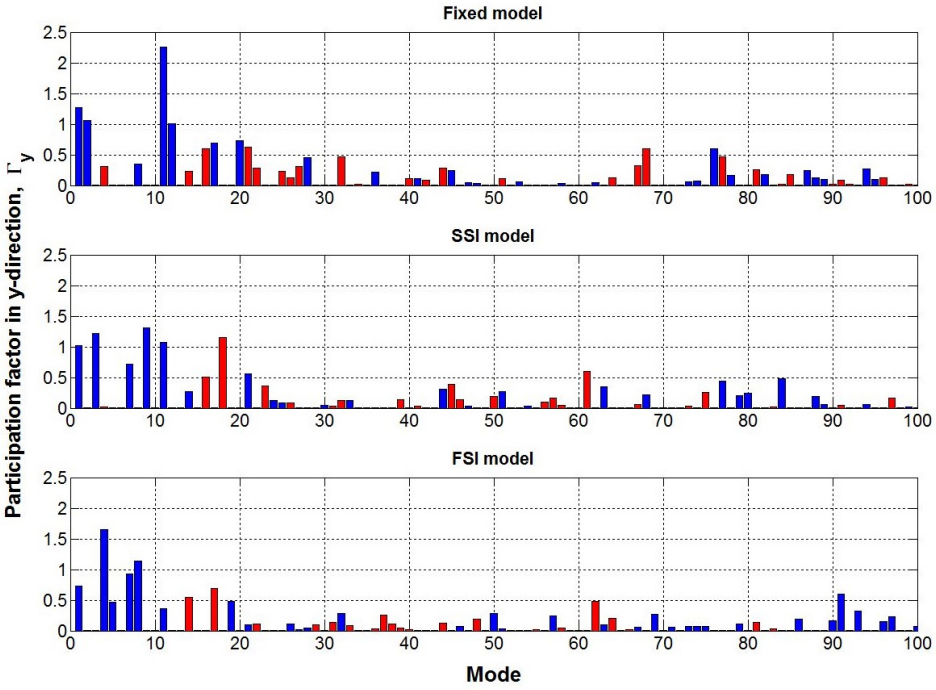

Figure 37: Participation factors of the first 100 modes in the y-direction for the three models.

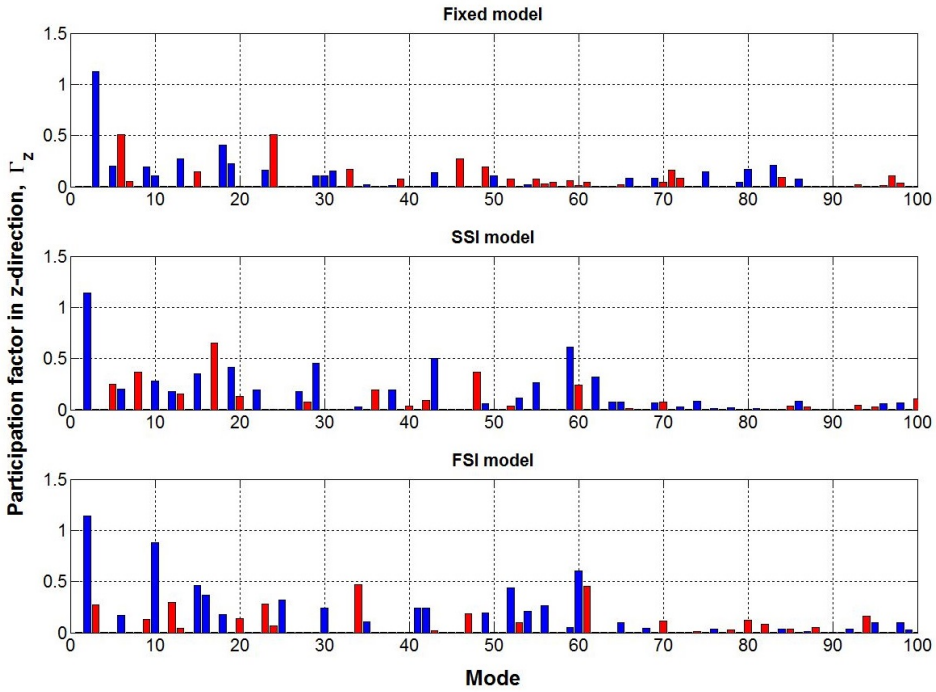

Figure 38: Participation factors of the first 100 modes in the z-direction for the three models.

D Displacement histories g by direct implicit integration

Below in figures 39, 40 and 41 are the displacement histories for the three models of the HTT PS obtained by direct, implicit integration. The acceleration time series used are those obtained for the Åsgård field.

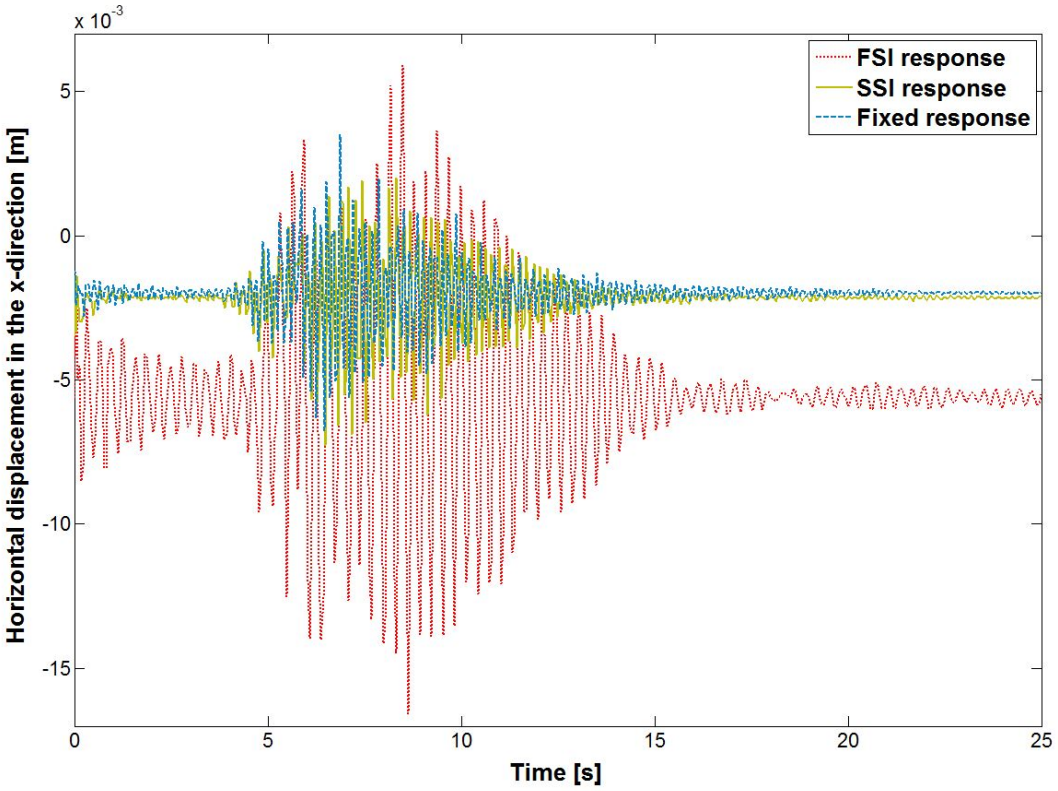

Figure 39: Horizonal displacement history in x-direction.

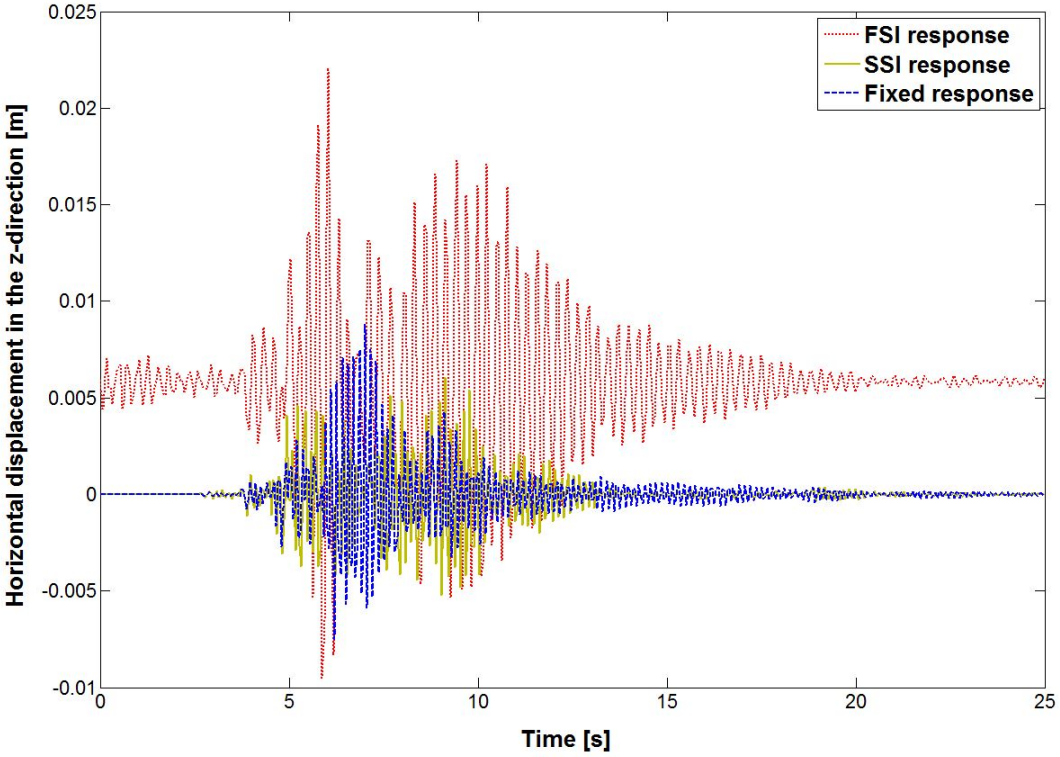

Figure 40: Horizonal displacement history in z-direction.

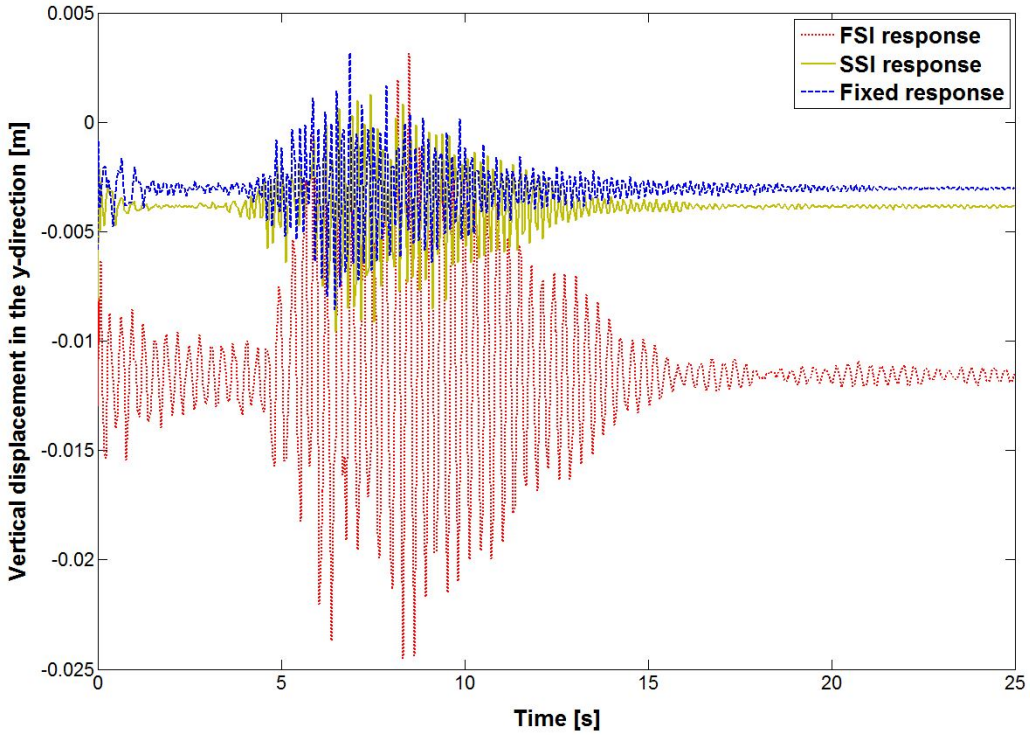

Figure 41: Vertical displacement history (y-direction).

E Displacement histories generated by modal analysis

Utilizing the Åsgård acceleration time series the modal analysis of the HTT PS rendered the displacement histories shown in figures 42, 43 and 44. They are plotted with the nonlinear analysis, the green dotted line, to point out the large difference in amplitude.

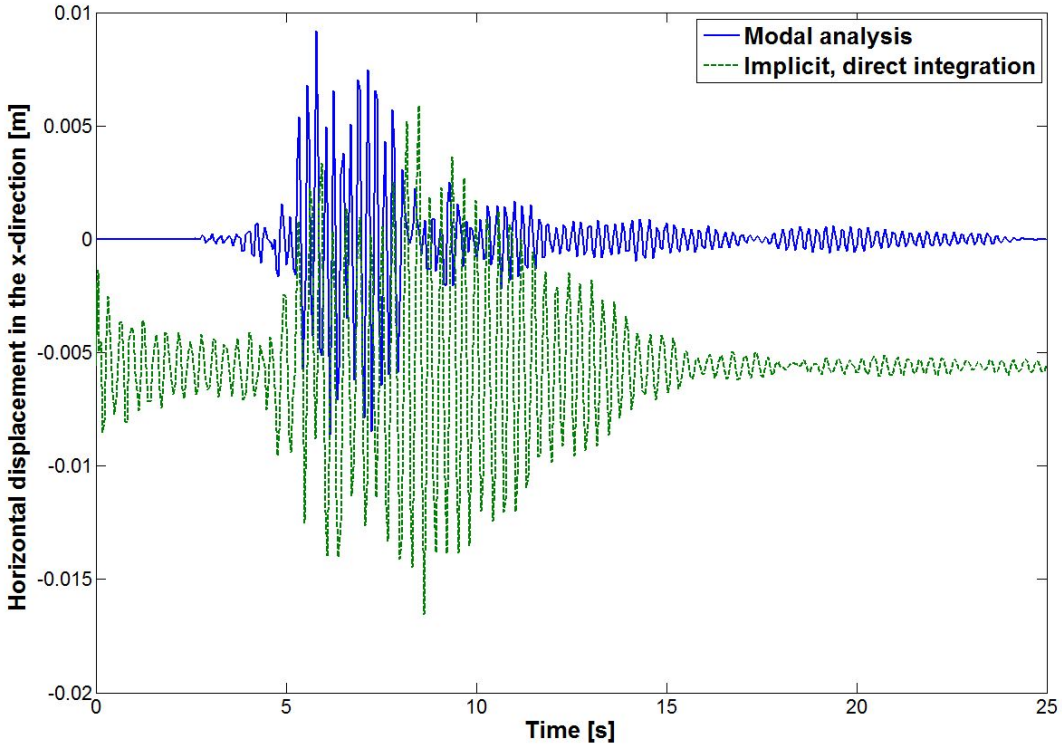

Figure 42: Horizontal displacement history in the x-direction.

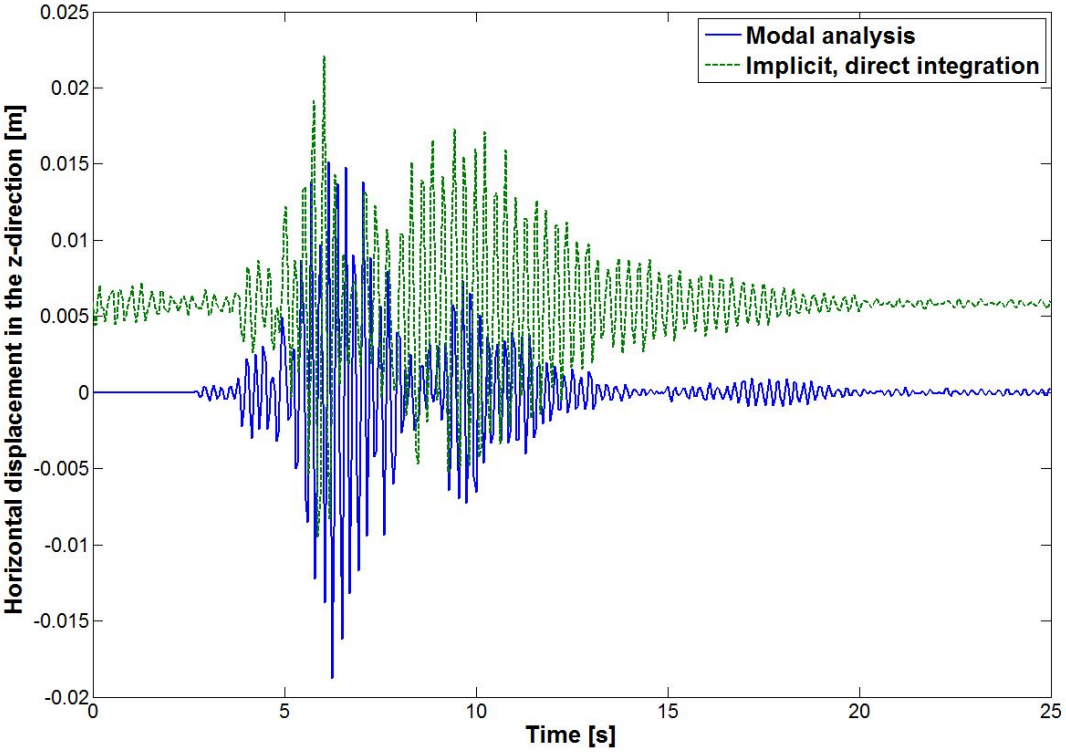

Figure 43: Horizontal displacement history in the z-direction.

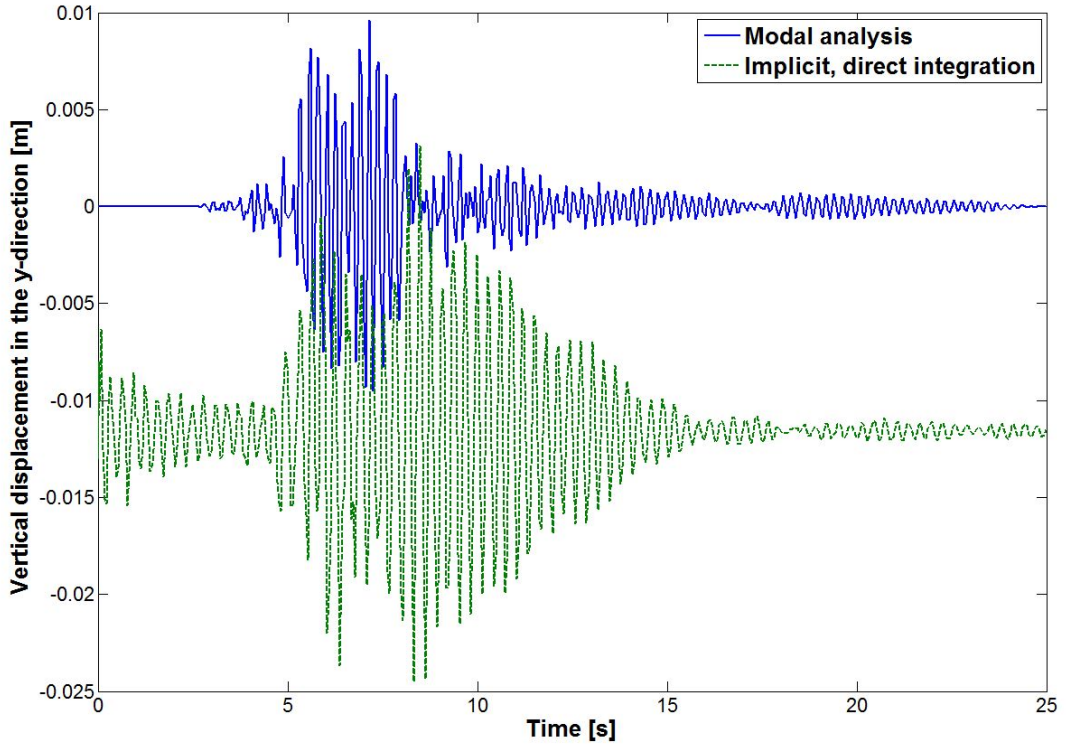

Figure 44: Vertical displacement history in the y-direction.

F Displacement histories for the Friuli acceleration time series.

Below in figures 45, 46 and 47 are the displacement histories for the HTT PS, the FSI version, generated by the Friuli acceleration time series presented. The displacement histories found by the Icelandic earthquake excitation are depicted as the yellow dotted line for comparison.

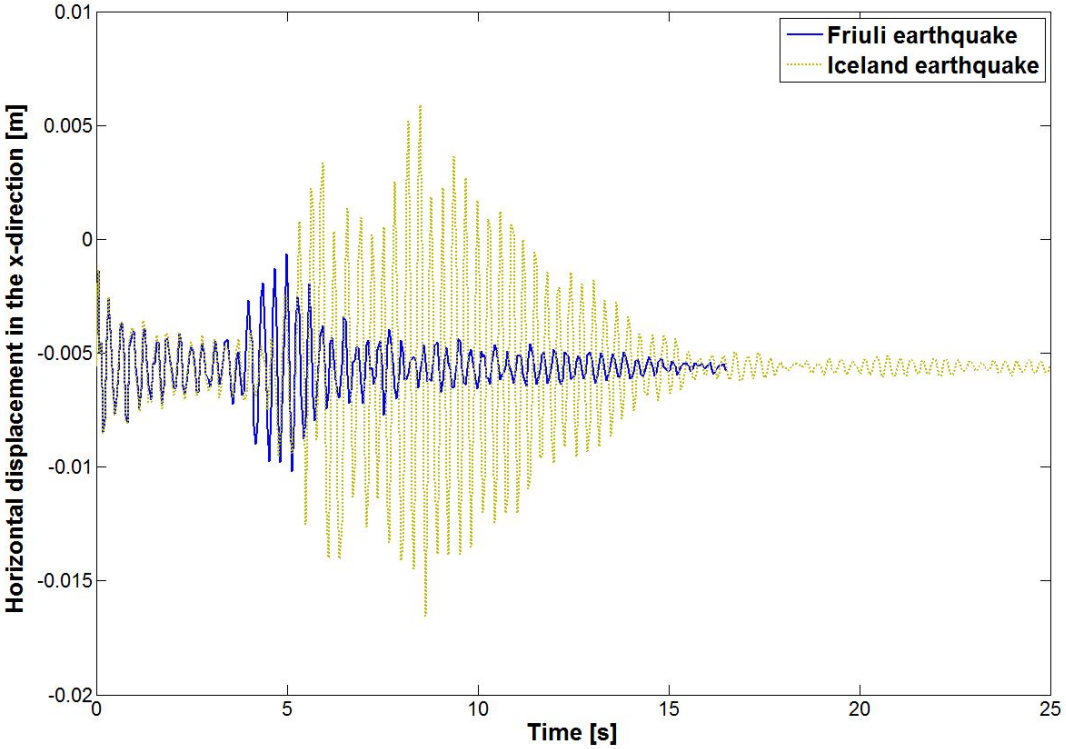

Figure 45: Horizontal displacement history in the x-direction.

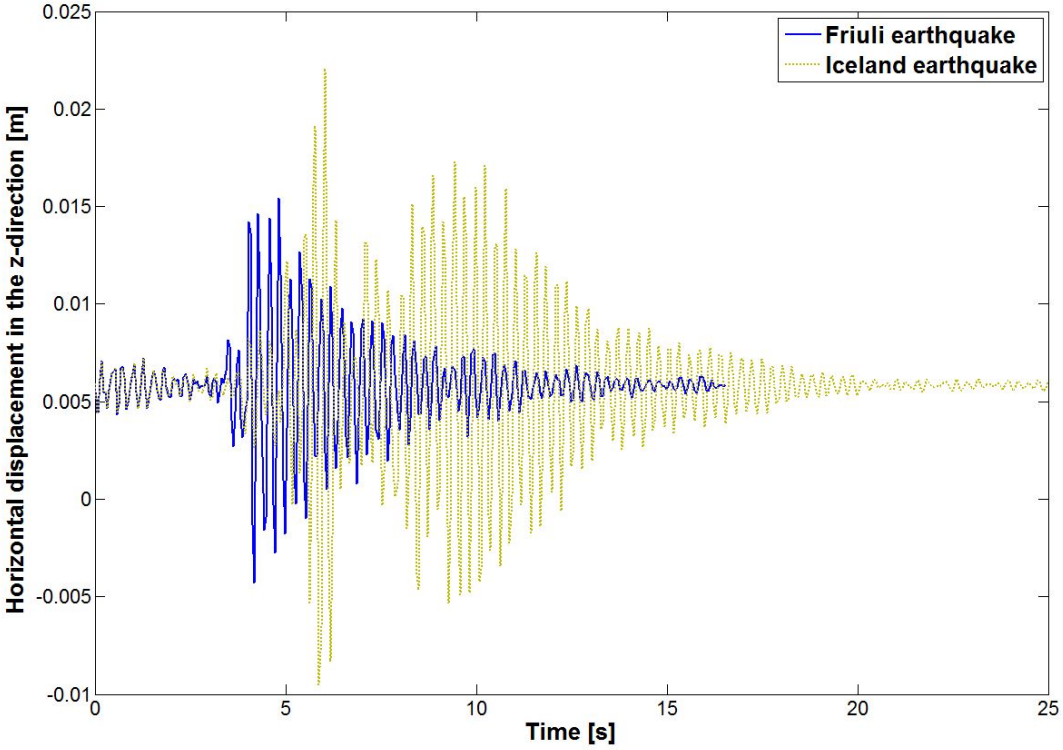

Figure 46: Horizontal displacement history in the z-direction.

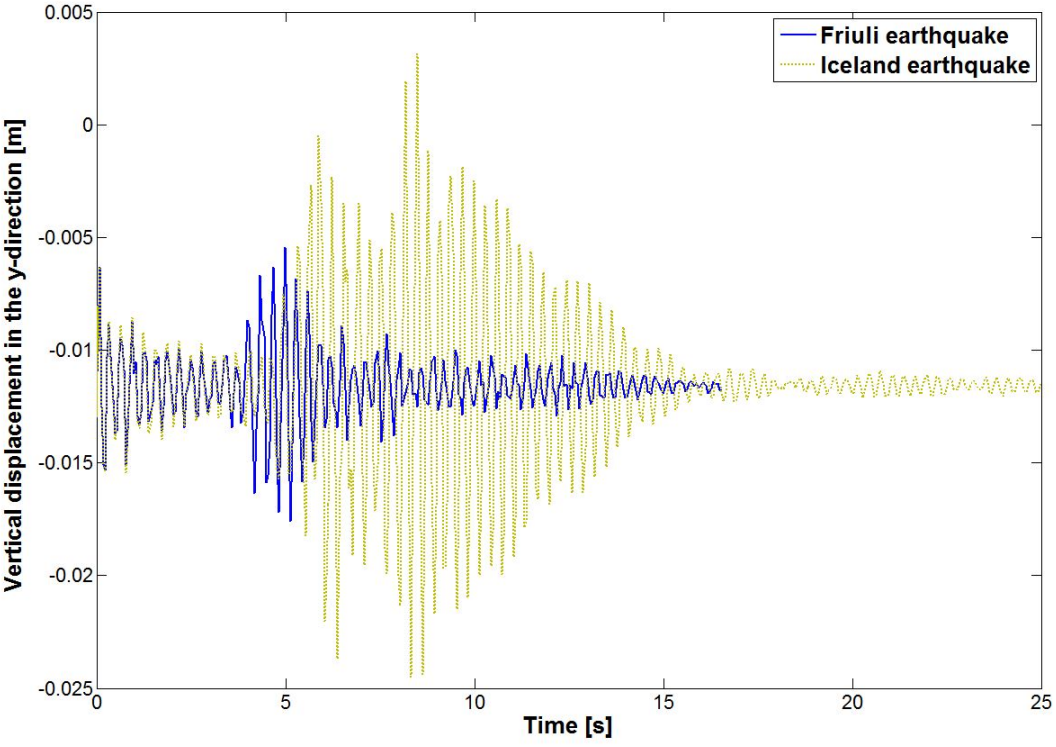

Figure 47: Vertical displacement history in the y-direction.

G Guide to the digital attachments

For the part of the digital attachment that concerns the generation of earthquake time series, a guide to the main scripts will be provided here.

G.1 The main file

The main file, "*ExtractMedian.m*" renders the earthquake for which the ten thousand year PGA is found. If another return perdiod is of interest, the parameter "s" can be changed. "*Loopnumber*" is the number of times one wishes to run the simulaton.

Further the synthetic earthquake catalogue is generated by "*EarthquakeCatalogue.m*" and the PGA-values for the selected site are computed for each of the earthquakes in the earthquake catalogue in the script "*ResponseCalculation.m*". The parameter one wishes to perform extreme value statistics on is defined next, and the 10 000 largest values computed for this parameter is chosen as basis for the extreme value evaluation. Next the input variables for the extreme value evaluation are chosen (explained in the script "*EstimateEVD.m*") and the file "*OrderStatistics.m*" will provide the parameter corresponding to the chosen return period. For each run the parameter is stored along with the appurtenant data used to describe the earthquake at which it originates from.

G.2 EarthquakeCatalogue.m

The script "*EarthquakeCatalogue.m*" generates the synthetic earthquake catalogue. It runs the script "DefineSourceZones" which contains the coordinates of the source zones, the id provided in the zonation report [4], the Gutenberg-Richter parameters and the range for the magnitude of the earthquake.

Next the magnitudes and the number of earthquakes for each zone is computed in "*MagnitudeSimulation.m*". Further, "*EpicentreSimulation.m*" generates the epicentres defined within a rectangle. The epicentres that lies within the polygon is then extracted by "*Polygon.m*". Then the generated earthquakes are stored in the variable "*data*" and further on this variable is stored in a more structured way by "$EQ_Data Structure.m$".

G.3 ResponseCalculation.m

In "*ResponseCalculation.m*" the coordinates of the site is first specified. Next the attenuation relation introduced in chapter 3.2 is used in the scripts "$GMEE_hPGA_2005.m$", "$GMEE_vPGA_2005.m$", "$GMEE_hSa_2005.m$" and "$GMEE_vSa_2005.m$" to estimate the ground motion parameter.

G.4 OrderStatistics.m

For the chosen input values order statistics are performed on the chosen parameter in "*OrderStatistics.m*". The script "*EstimateEVD.m*" calculates the parameter corresponding to the chosen return period and plots the distribution of this parameter. The maximum value in this distribution is stored in the variable "*EQuse*" which is stored in a text file referring to the main script each time the simulation is run.